

ASTROMETRIC MICROLENSING BY LOCAL DARK MATTER SUBHALOS

ADRIENNE L. ERICKCEK^{1,2} AND NICHOLAS M. LAW³
Draft version August 17, 2018

ABSTRACT

High-resolution N-body simulations of dark matter halos indicate that the Milky Way contains numerous subhalos. When a dark matter subhalo passes in front of a star, the light from that star will be deflected by gravitational lensing, leading to a small change in the star's apparent position. This astrometric microlensing signal depends on the inner density profile of the subhalo and can be greater than a few microarcseconds for an intermediate-mass subhalo ($M_{\text{vir}} \gtrsim 10^4 M_{\odot}$) passing within arcseconds of a star. Current and near-future instruments could detect this signal, and we evaluate the Space Interferometry Mission's (SIM's), Gaia's, and ground-based telescopes' potential as subhalo detectors. We develop a general formalism to calculate a subhalo's astrometric lensing cross section over a wide range of masses and density profiles, and we calculate the lensing event rate by extrapolating the subhalo mass function predicted by simulations down to the subhalo masses potentially detectable with this technique. We find that, although the detectable event rates are predicted to be low on the basis of current simulations, lensing events may be observed if the central regions of dark matter subhalos are more dense than current models predict ($\gtrsim 1 M_{\odot}$ within 0.1 pc of the subhalo center). Furthermore, targeted astrometric observations can be used to confirm the presence of a nearby subhalo detected by gamma-ray emission. We show that, for sufficiently steep density profiles, ground-based adaptive optics astrometric techniques could be capable of detecting intermediate-mass subhalos at distances of hundreds of parsecs, while SIM could detect smaller and more distant subhalos.

Subject headings: astrometry – dark matter – Galaxy:halo – gravitational lensing:micro

1. INTRODUCTION

Numerical simulations of dark matter halos have revealed the presence of numerous subhalos over a wide range of masses extending down to the simulations' resolution limits (e.g., Ghigna et al. 1998, 2000; Klypin et al. 1999a; Moore et al. 1999; Kravtsov et al. 2004; Gao et al. 2004; Reed et al. 2005; Diemand et al. 2007b; Springel et al. 2008; Diemand et al. 2008). This substructure is the remnant of hierarchical structure formation; as halos merge to form larger structures, the inner portions of the ancestor halos become subhalos. If all halos leave subhalo remnants, then the subhalo mass function may extend to masses far smaller than the resolution limit of any simulation (Hu et al. 2000; Chen et al. 2001; Profumo et al. 2006; Diemand et al. 2005).

Although subhalos may be destroyed by gravitational interactions with the host halo, other subhalos, and stars, there are indications that their dense inner regions survive to the present day (Hayashi et al. 2003; Kazantzidis et al. 2004; van den Bosch et al. 2005; Read et al. 2006; Berezhinsky et al. 2006; Zhao et al. 2007; Green & Goodwin 2007; Goerdt et al. 2007; Schneider et al. 2010; Ishiyama et al. 2010). Moreover, high-resolution simulations of halos similar to the Milky Way's host suggest that subhalos with masses greater than $10^6 M_{\odot}$ are present at the Solar radius (Springel et al. 2008; Diemand et al. 2008). Although simulations indicate that these large subhalos are significantly disrupted by the Galactic disk (D'Onghia et al. 2010; Romano-Díaz et al. 2010), the resolution is not sufficient to determine the fate of the sub-

halos' innermost regions. It is therefore possible that numerous subhalos are located within a few kiloparsecs of the Solar System, with profound implications for both direct detection of the dark matter particle (Kamionkowski & Koushiappas 2008) and indirect detection through its annihilation signature (e.g., Bergström et al. 1999; Calcáneo-Roldán & Moore 2000; Stoehr et al. 2003; Diemand et al. 2007a; Ando 2009; Kamionkowski et al. 2010).

Unfortunately, both indirect and direct detection of dark matter continues to be elusive, and gravity still provides the only uncontested evidence for dark matter. Gravitational lensing is an especially powerful tool in the study of dark matter substructure; subhalos within our galaxy could be detected through their effects on signals from millisecond pulsars (Siegel et al. 2007), and substructure in lensing galaxies has several observational signatures. Subhalos have been proposed as the origin of observed flux-ratio anomalies between the multiple images of strongly lensed quasars (Mao & Schneider 1998; Metcalf & Madau 2001; Chiba 2002; Dalal & Kochanek 2002; Kochanek & Dalal 2004); they can also alter the time delays between these images (Keeton & Moustakas 2009; Congdon et al. 2010) and their separations (Koopmans et al. 2002; Chen et al. 2007; Williams et al. 2008; More et al. 2009). If the source is extended, then subhalos can distort the image's shape and surface brightness (Metcalf 2002; Inoue & Chiba 2005a,b; Koopmans 2005; Vegetti & Koopmans 2009a,b). Intriguingly, the observed lensing anomalies can only be explained if the central regions of the lensing galaxies contain significantly more substructure than is predicted by n-body simulations (Mao et al. 2004; Amara et al. 2006; Macciò et al. 2006; Xu et al. 2009, 2010), although it has been suggested that these studies use atypical lensing galaxies (Bryan et al. 2008; Jackson et al. 2010).

Individual subhalos within a lensing galaxy could be de-

¹ Canadian Institute for Theoretical Astrophysics, University of Toronto, 60 St. George Street, Toronto, Ontario M5S 3H8, Canada; erickcek@cita.utoronto.ca

² Perimeter Institute for Theoretical Physics, 31 Caroline St. N, Waterloo, Ontario N2L2Y5, Canada

³ Dunlap Fellow, Dunlap Institute for Astronomy and Astrophysics, University of Toronto, 50 St. George Street, Toronto ON M5S 3H4, Canada

ected if they strongly lens one quasar image, splitting it into a closely spaced pair of images (Yonehara et al. 2003; Inoue & Chiba 2005a). Unfortunately, the diffuse nature of dark matter subhalos implies that they have small Einstein radii (Zackrisson et al. 2008). Consequently, the split images are resolvable only for the largest subhalos, making it unlikely to find a large enough subhalo with a sufficiently small impact parameter to detectably split a quasar image (Riehm et al. 2009).

In this paper, we consider a different way to find subhalos through gravitational lensing: instead of looking for split images, we investigate how the astrometric deflection of an image changes as a subhalo moves. This astrometric microlensing approach has two advantages over strong lensing. First, it is much easier to measure a change in the position of the centroid of an image than it is to resolve an image pair into distinct sources. The minimal separation required to resolve a pair of images is limited to approximately the resolution of the telescope ($\gtrsim 25$ mas), whereas at high signal-to-noise ratio (S/N), the position of the centroid of the image can be measured with hundreds of times higher precision. Second, strong lensing only occurs when the angular separation between the source and the lens is smaller than the lens’s Einstein angle, while astrometric deflection is detectable for far larger impact parameters. The disadvantage associated with astrometric microlensing is that it must be a dynamical event because we do not know the true position of the source. As the lens moves relative to a background star, the star’s image will move as well, and that is the detectable signature of astrometric microlensing. We are therefore constrained to local subhalos with significant proper motions.

Astrometric lensing signals from dark matter subhalos are necessarily small because subhalos are diffuse, and astrometry has only very recently progressed to the point that an astrometric dark matter search is feasible. The rapid development of 1-100 μ as astrometric precision has been driven by a wide variety of fields – for example, following orbits in the galactic center (e.g., Lu et al. 2009; Gillessen et al. 2009); astrometric detection of planets (e.g., Unwin et al. 2008; Law et al. 2009; Malbet et al. 2010); accurate parallax determination (e.g., Henry et al. 2009; Subasavage et al. 2009); and the determination of stellar orbits (e.g., Helminiak et al. 2009; Pravdo et al. 2006; Konopacky et al. 2010; Ireland et al. 2008; Dupuy et al. 2009).

New space-based astrometric missions such as Gaia (Lindgren et al. 2008) and SIM (Unwin et al. 2008) are opening the possibility of ultra-high-precision all-sky and targeted searches. Targeted ground-based astrometry is already capable of 100 μ as precision in arcminute-sized fields, and new larger telescopes will significantly improve that precision (Cameron et al. 2009), while even higher precisions are possible on bright stars (e.g., Muterspaugh et al. 2006; van Belle et al. 2008).

These technical advances have inspired considerable interest in astrometric microlensing by stars and dark compact objects (Walker 1995; Paczynski 1995, 1998; Miralda-Escude 1996; Gould 2000; Gaudi & Bloom 2005), and by baryonic clouds (Takahashi 2003; Lee et al. 2010). In this paper, we investigate if these instruments can also be used to search for dark matter subhalos. We find that, for standard dark matter models, observing a subhalo lensing event rate during a blind astrometric survey is highly unlikely. If the central regions of dark matter subhalos are denser than expected, however, the lensing event rate can be significantly enhanced. We also

explore the possibility of using astrometric lensing to confirm the presence of a subhalo detected through its gamma-ray emission. We find that ground-based telescopes could detect lensing by a nearby (~ 50 pc) subhalo with a post-stripping mass greater than $1000 M_{\odot}$, while SIM could probe these subhalos at greater distances (~ 100 pc) and detect nearby subhalos with one-tenth of this mass.

This article is organized as follows. In Section 2, we describe the image motion induced by subhalo lenses with a variety of different density profiles, namely, a singular isothermal profile, the NFW profile, and a generalized power-law density profile. In Section 3, we develop an astrometric observing strategy designed to reliably detect subhalo lensing while rejecting possible false-positive detections. In Section 4, we calculate the areas of sky over which particular subhalo lenses are detectable and determine the all-sky subhalo lensing event rates for several models of dark matter substructure. In Section 5, we evaluate current and planned astrometric survey capabilities in the context of detecting lensing from a subhalo in both all-sky and targeted searches. We summarize our findings and conclude in Section 6. To evaluate the lensing signatures and event rates, we developed models of the concentration-mass relation and the mass function for local subhalos based on the findings of the Aquarius simulations (Springel et al. 2008); these models are presented in the appendix.

2. ASTROMETRIC SIGNATURES OF LENSING BY SUBHALOS

The shapes of the intermediate-mass subhalos that we will be considering cannot be probed by current numerical simulations; to simplify our analysis we will assume that the subhalos are spherically symmetric. Numerical simulations can only probe the shapes of the largest subhalos with masses greater than $10^8 M_{\odot}$ (Kuhlen et al. 2007; Knebe et al. 2010). While these subhalos are triaxial, they tend to be more spherical than their host halos. In a simulation that includes baryonic physics, Knebe et al. (2010) found that subhalos located within half of the virial radius of the host halo have nearly spherical mass distributions in their innermost resolved regions, with a median minor-to-major axis ratio of 0.83. We will see that astrometric microlensing is only sensitive to the density profile near the center of the subhalo ($r < 0.1$ pc); as long as the inner region of the subhalo is nearly spherically symmetric, the subhalo’s triaxiality is irrelevant for our analysis, and we do not expect deviations from spherical symmetry to significantly affect our results.

We will also assume that the dark matter subhalo is transparent and that it contains no stars. The presence of a star in the center of the subhalo would change its lensing signature if the star’s mass is comparable to the dark matter mass in the central 0.1 pc of the subhalo, but stars further from the center would not have an effect. Furthermore, the discrepancy between the number of intermediate-mass subhalos seen in simulations and the number of dwarf spheroidal objects observed in the Milky Way, known as the “missing satellite problem” (Klypin et al. 1999b; Moore et al. 1999), indicates that stars are rare in subhalos with masses less than $10^6 M_{\odot}$ (Madau et al. 2008). Finally, we will assume that the subhalo’s diameter is small compared to both the distance d_L between the lens and the observer and the distance d_{LS} between the lens and the star.

Figure 1 shows a schematic view of lensing by an extended transparent object like a dark matter subhalo. When a light ray passes through a spherically symmetric thin lens, the image of

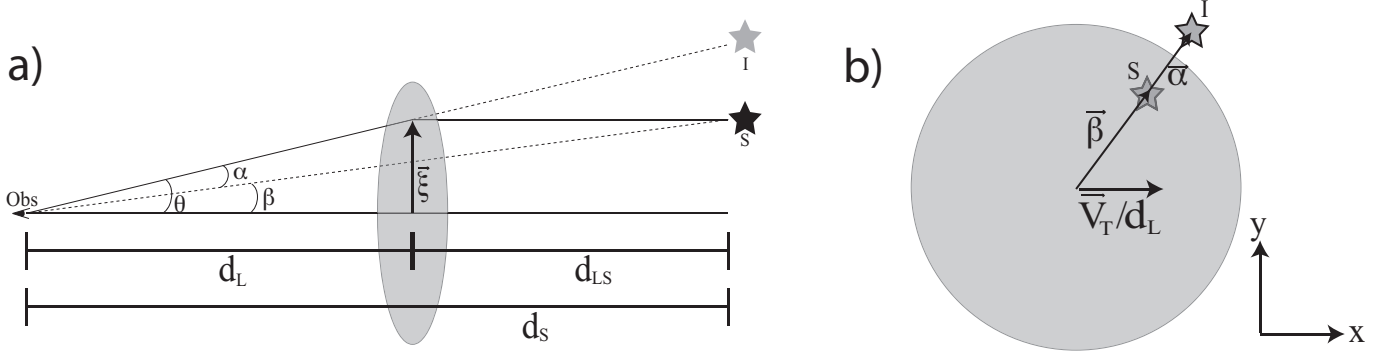


FIG. 1.— a) Diagram showing the position of the source star (in black), its image (in gray), and the lens (gray ellipse). We will generally assume that $\alpha \ll \beta$ so that the ray's impact parameter in the lens plane ($\xi \equiv d_L \theta$) may be approximated as $\xi \approx d_L \beta$. b) The same lensing system viewed as projected on the sky. The center of the lens is moving with velocity v_T along the x -axis.

the star is shifted from its true position by an angle

$$\vec{\alpha} = \frac{d_{LS}}{d_S} \left[\frac{4GM_{2D}(\xi)}{\xi} \right] \hat{\xi}, \quad (1)$$

where d_S is the distance between the observer and the star, ξ is the distance between the center of the lens and the star's image in the lens plane ($\xi \equiv d_L \theta$), and $\hat{\xi} \equiv \xi/\xi$ points from the lens to the star. Throughout this work, we set the speed of light $c = 1$. The mass $M_{2D}(\xi)$ in Eq. (1) is the mass enclosed by the cylinder interior to ξ and is obtained by integrating the projected surface mass density Σ over the area of the circle with radius ξ .

As the subhalo moves relative to the background star, the angle β that extends from the lens to the star will change, and the position of the star's image will change accordingly. We take the star to be fixed at the origin of an xy coordinate system on the sky, and we define the x -axis to be parallel to the subhalo's transverse velocity v_T , as shown in the right panel of Fig. 1. The vertical component of $\vec{\beta}$ is therefore fixed [$\beta_y(t) = \beta_{y,0}$], and

$$\beta_x(t) = \beta_{x,0} - 4.2'' \left(\frac{v_T}{200 \text{ km/s}} \right) \left(\frac{50 \text{ pc}}{d_L} \right) \left(\frac{t}{5 \text{ yr}} \right), \quad (2)$$

where $\beta_{x,0}$ is the value of β_x at $t = 0$. We see that a nearby subhalo will move several arcseconds during a multi-year observational period.

For the subhalos we consider, the deflection angle α will be on the order of microarcseconds. Since β changes by several arcseconds over the course of the observation, $\beta \gg \alpha$ for most of the observational period. We will further assume that $\beta_{y,0} \gg \alpha$ so that we are always considering the weak-lensing regime with $\beta \gg \alpha$. We verify in Appendix A that this condition is satisfied for all subhalo lensing scenarios, provided that $d_L \ll 1000$ kpc. This confirms that we are firmly in the weak lensing regime as long as we only consider subhalos in our local group. In this case, there is only one image of the star, and it is always located on the line connecting the lens position to the star's position, with the star between the image and the lens. We will use the $\beta \gg \alpha$ assumption to simplify the lens equation by approximating $\vec{\beta} \approx \vec{\theta}$. In this case, $\vec{\xi}$ may be approximated as $\vec{\xi} \approx d_L \vec{\beta}$, and Eq. (1) becomes a simple equation for the deflection angle $\vec{\alpha}$ in terms of the impact parameter $\vec{\beta}$. In the following subsections, we will use Eq. (1) to show how the path taken by the star's image during a subhalo transit depends on the subhalo's density profile.

2.1. Singular isothermal sphere

The density profile for a singular isothermal sphere (SIS) is

$$\rho(r) = \frac{\sigma_v^2}{2\pi G r^2}, \quad (3)$$

where σ_v is the velocity dispersion of the halo. Although numerical simulations indicate that large dark matter subhalos without baryons do not have this steep a density profile (Springel et al. 2008; Diemand et al. 2008), we consider the SIS case in detail because it simply illustrates key features that are shared by the astrometric lensing signatures from dark matter halos with shallower profiles.

The two-dimensional enclosed mass for an infinite SIS is $M_{2D}(\xi) = \pi \sigma_v^2 \xi / G$. Since M_{2D} depends linearly on ξ , Eq. (1) reveals that α is independent of the separation between the lens and the star. The deflection angle is always the Einstein angle of the SIS:

$$\theta_E^{\text{SIS}} = \left(1 - \frac{d_L}{d_S} \right) 4\pi \sigma_v^2, \quad (4)$$

$$= 10 \mu\text{as} \left(\frac{\sigma_v}{0.6 \text{ km/s}} \right)^2 \left(1 - \frac{d_L}{d_S} \right). \quad (5)$$

There are two images, with $\vec{\alpha} = \pm \theta_E^{\text{SIS}} \hat{\beta}$, only if $\beta < \theta_E^{\text{SIS}}$. We will only consider larger impact parameters, in which case there is only one image, with $\vec{\alpha} = \theta_E^{\text{SIS}} \hat{\beta}$. As the SIS moves relative to the star, the direction of the deflection angle changes. For an infinite SIS moving from the distant left to the distant right, the image starts θ_E^{SIS} to the right of the star's true position and then traces a half-circle with radius θ_E^{SIS} until it ends θ_E^{SIS} to the left of the star's true position.

For an SIS, the mass enclosed in a sphere of radius R is proportional to R ; if the SIS has infinite extent, then its mass is infinite. It is customary to characterize an SIS by its virial mass: the mass contained in a sphere with mean density equal to the virial density $\bar{\rho}_{\text{vir}}$. Bryan & Norman (1998) provide a fitting formula for the virial density in a flat Λ CDM universe,

$$\bar{\rho}_{\text{vir}} \equiv \left(18\pi^2 + 82[\Omega_M(z) - 1] - 39[\Omega_M(z) - 1]^2 \right) \rho_{\text{crit}}, \quad (6)$$

$$\Omega_M(z) = \frac{\Omega_{M0}(1+z)^3}{\Omega_{M0}(1+z)^3 + 1 - \Omega_{M0}}, \quad (7)$$

$$\rho_{\text{crit}}(z) = \left(0.0924 \frac{M_{\oplus}}{\text{pc}^3} \right) h^2 \left[\Omega_{M0}(1+z)^3 + 1 - \Omega_{M0} \right], \quad (8)$$

where $H_0 \equiv 100h \text{ km s}^{-1} \text{ Mpc}^{-1}$ and Ω_{M0} is the present-day

matter density divided by the critical density. We will use standard cosmological parameters: $h = 0.7$ and $\Omega_{M0} = 0.3$. The virial density is $4.6 M_{\oplus} \text{pc}^{-3}$ at redshift zero and it increases monotonically with redshift. The velocity dispersion σ_v in terms of the virial mass is

$$\sigma_v^2 = G \left(\frac{\pi \bar{\rho}_{\text{vir}}(z_v) M_{\text{vir}}^2}{6} \right)^{1/3}, \quad (9)$$

where z_v is the redshift at which the halo's virial mass is evaluated. To facilitate comparisons with N-body simulations, we take $z_v = 0$ in our calculations, but we note that increasing z_v would make the subhalos denser and would enhance their lensing signals. Inserting this expression into Eq. (4) gives

$$\theta_E^{\text{SIS}} = (1.1 \mu\text{as}) \left(1 - \frac{d_L}{d_S} \right) \left(\frac{M_{\text{vir}}}{10^4 M_{\odot}} \right)^{2/3} \left(\frac{\bar{\rho}_{\text{vir}}(z_v)}{4.6 M_{\oplus} \text{pc}^{-3}} \right)^{1/3}. \quad (10)$$

These properties describe an SIS in isolation. Once a subhalo is accreted by a larger halo, the outer tails of its density profile are stripped of mass. Numerical simulations indicate that a subhalo in our Galaxy may lose between 99% and 99.9% of its initial mass due to tidal stripping from the smooth component of the halo (Hayashi et al. 2003; Kazantzidis et al. 2004; van den Bosch et al. 2005; Read et al. 2006), and stars will further strip the outer portions of subhalos (Berezinsky et al. 2006; Zhao et al. 2007; Green & Goodwin 2007; Goerdet et al. 2007; Schneider et al. 2010; Ishiyama et al. 2010). We will deal with this truncation by defining a truncation radius R_t and setting $\rho = 0$ for $R > R_t$. The mass contained within R_t is the mass of the surviving subhalo M_t . We will describe the tidal stripping with the parameter $m_{\text{bd}} \equiv M_t/M_{\text{vir}}$, where M_{vir} is the original virial mass of the subhalo, evaluated at redshift z_v . The truncation radius is then given by

$$R_t = (0.56 \text{ pc}) \left(\frac{m_{\text{bd}}}{0.001} \right) \left(\frac{M_{\text{vir}}}{10^4 M_{\odot}} \right)^{1/3} \left(\frac{4.6 M_{\oplus} \text{pc}^{-3}}{\bar{\rho}_{\text{vir}}(z_v)} \right)^{1/3}. \quad (11)$$

The angular size of the truncated halo is

$$\theta_t = 0.64^\circ \left(\frac{m_{\text{bd}}}{0.001} \right) \left(\frac{50 \text{ pc}}{d_L} \right) \left(\frac{M_{\text{vir}}}{10^4 M_{\odot}} \right)^{1/3} \left(\frac{4.6 M_{\oplus} \text{pc}^{-3}}{\bar{\rho}_{\text{vir}}(z_v)} \right)^{1/3}. \quad (12)$$

Thus we see that $\theta_E^{\text{SIS}} \ll \theta_t$ for all subhalos of interest.

For a truncated SIS, the two-dimensional enclosed mass is

$$M_{2D}(\xi < R_t) = \frac{2\sigma_v^2}{G} \left[\xi \tan^{-1} \sqrt{\frac{R_t^2}{\xi^2} - 1} + R_t - \sqrt{R_t^2 - \xi^2} \right] \quad (13)$$

and $M_{2D} = M_t$ for $\xi \geq R_t$. If $\xi \geq R_t$, then the deflection angle is the same as for a point mass with Einstein angle

$$\theta_E^{\text{PM}} \equiv \sqrt{\frac{4GM_t d_{LS}}{d_L d_S}} = \sqrt{\frac{2}{\pi} \theta_E^{\text{SIS}} \theta_t}. \quad (14)$$

Thus we see that $\theta_E^{\text{SIS}} \ll \theta_t$ implies that $\theta_E^{\text{PM}} \ll \theta_t$. Therefore we may approximate the position of the brightest image as $\alpha = (\theta_E^{\text{PM}})^2/\beta$ for $\beta > \theta_t$. When we insert M_{2D} from Eq. (13) into Eq. (1) for α and assume that $\alpha \ll \beta$, we find that the deflection angle for lensing by a truncated SIS is

$$\vec{\alpha} = \frac{2}{\pi} \theta_E^{\text{SIS}} \hat{\beta} \begin{cases} \mathcal{F}\left(\frac{\beta}{\theta_t}\right) & \text{for } \theta_E^{\text{SIS}} < \beta < \theta_t, \\ \frac{\theta_t}{\beta} & \text{for } \beta > \theta_t \end{cases}, \quad (15)$$

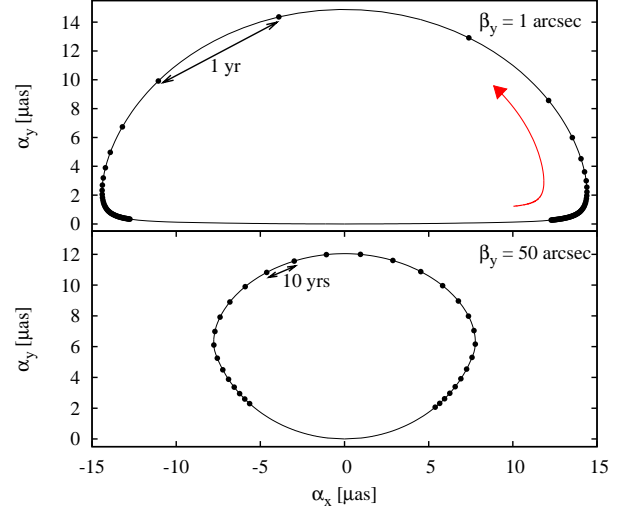


FIG. 2.— The deflection angle for a star at 5 kpc as an SIS subhalo 50 pc away moves at a velocity of 200 km/s from the far left to the far right. This subhalo's velocity dispersion is 0.72 km/s, which corresponds to a virial mass of $5 \times 10^5 M_{\odot}$, but it has been stripped to a radius of 0.02 pc and contains only $5 M_{\odot}$. In the top plot, the subhalo center passes 1 arcsecond below the star, and the circles show the image's position every year for the 100 years surrounding the time of closest approach. In the bottom plot, the subhalo center passes 50 arcseconds below the star, and the circles show the image's position every 10 years for the 300 years surrounding the time of closest approach.

$$\mathcal{F}(x) \equiv \tan^{-1} \sqrt{\frac{1}{x^2} - 1} + \frac{1}{x} - \sqrt{\frac{1}{x^2} - 1}.$$

Figure 2 shows how the image of a fixed star moves as a truncated SIS subhalo passes below the star's true position on the sky. The lens's Einstein angle is $\theta_E^{\text{SIS}} = 15 \mu\text{as}$, which corresponds to $\sigma_v = 0.72 \text{ km/s}$ and $M_{\text{vir}} = 5 \times 10^5 M_{\odot}$. The image motion is highly sensitive to the ratio v_T/d_L because this ratio determines how $\vec{\beta}$ changes with time [see Eq. (2)]. If v_T/d_L is decreased, then the change in $\vec{\beta}$ during a set time interval is decreased, and the image motion slows down. Throughout this work, we adopt $v_T = 200 \text{ km/s}$ because that is the typical velocity of a dark matter particle in the halo (e.g., Drukier et al. 1986; Xue et al. 2008). With this velocity, we will see that a detectable subhalo must have $d_L \lesssim 100 \text{ pc}$, and we adopt $d_L = 50 \text{ pc}$ as our fiducial lens distance. Provided that $d_L \ll d_S$, the distance to the source has a minimal impact on the image motion because d_S only enters through the factor $(1 - d_L/d_S)$ in θ_E^{SIS} [see Eq. (10)]. We use $d_S = 5 \text{ kpc}$ as our fiducial value because this is a reasonable distance to a target star; changing d_S to any value greater than 1 kpc would have no noticeable effect on the image motion. To illustrate the effects of subhalo truncation in Fig. 2, we assume that the subhalo has been extremely stripped by close encounters with stars so that its radius is 0.02 pc ($\theta_t = 85''$), which implies that $M_t = 5 M_{\odot}$. We see that the image motion consists of three stages: as the edge of the subhalo approaches from the far left, the image very slowly moves rightward until the star is behind the subhalo, then the image rapidly traces an arc as the subhalo center passes by the star, and finally the star slowly returns to its true position as the subhalo moves off to the right.

The impact parameter β_y determines how quickly the image moves as the subhalo passes by the star. In the top half of Fig. 2 the lens impact parameter is $1''$, and the image rapidly

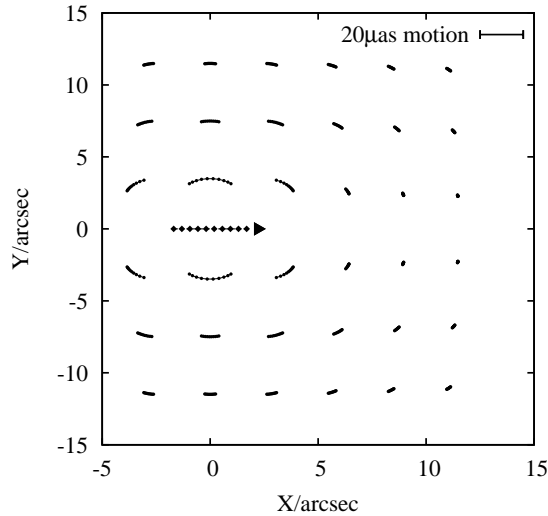


FIG. 3.— The deflection induced over 4 years by a moving SIS lens with the same properties as in Fig. 2. The path of the lens is depicted by a dotted arrow. To show the image trajectories, the image motion is exaggerated a factor of 10^6 relative to the star’s positions; a scale bar corresponding to $20\mu\text{as}$ motion is shown. Twenty equally spaced measurement points over the 4-year observational period are shown for each curve. Note that the stars closest to the lens position undergo much more rapid position changes.

traces out a semi-circle of radius θ_E^{SIS} during the few years surrounding the time of closest approach, just as if the lens had infinite extent. The effect of the SIS’s truncation is more apparent in the bottom half of Fig. 2, where $\beta_y = 50''$; the image’s trajectory is closer to a circle, and it will become more and more circular as β_y increases. The image transverses this circle very slowly, taking 10 years to move $2\mu\text{as}$, in contrast to the image in the top panel, which moves nearly $30\mu\text{as}$ in only 5 years. Thus we see that the only detectable portion of the image’s path in the sky is the period surrounding the moment of closest approach between the star and the lens, and a small impact parameter is required to make the image move significantly over the course of a few years. Figure 3 further illustrates the necessity of a small impact parameter by showing how the images of stars at different positions relative to the lens move over the course of 4 years; only the stars along the lens’s path with $\beta_y \lesssim 2''$ have images that are significantly moved during the observational period. For stars that are this close to the center of the subhalo, with $\beta \ll \theta_t$, the truncation of the density profile does not affect the image trajectories, as seen in the top panel of Fig. 2. We will therefore assume that $\beta \ll \theta_t$ for all interesting lensing scenarios and ignore the subhalo’s truncation when considering other density profiles.

2.2. NFW density profile

The NFW profile,

$$\rho(r) = \frac{\rho_s}{\left(\frac{r}{r_s}\right)\left(1 + \frac{r}{r_s}\right)^2}, \quad (16)$$

was found to be a universally good fit to the density profiles of galaxy and cluster halos in early numerical simulations (Navarro et al. 1996, 1997). The two-dimensional enclosed mass for a subhalo with virial mass M_{vir} and an NFW density profile with concentration $c \equiv R_{\text{vir}}/r_s$ is

$$M_{2\text{D}}(\xi) = \frac{M_{\text{vir}}}{\ln(1+c) - \frac{c}{1+c}} \mathcal{G}\left(\frac{\xi}{r_s}\right) \quad (17)$$

$$\mathcal{G}(x) = \ln \frac{x}{2} + \begin{cases} \frac{1}{\sqrt{1-x^2}} \cosh^{-1} \frac{1}{x} & \text{for } x < 1 \\ 1 & \text{for } x = 1 \\ \frac{1}{\sqrt{x^2-1}} \cos^{-1} \frac{1}{x} & \text{for } x > 1 \end{cases}$$

(Bartelmann 1996; Golse & Kneib 2002).

From Eq. (1), we see that the magnitude of the deflection angle α is proportional to $M_{2\text{D}}/\xi$. For the NFW profile, $\alpha \propto \xi$ if $r \ll r_s$, and $\alpha \propto \xi^{-1}$ if $r \gg r_s$. Therefore, as an NFW subhalo approaches a star, the deflection angle will increase until the star crosses the scale radius ($\xi \approx r_s$), and then it will decrease until the star crosses the subhalo center, at which point it will begin to increase again until the star crosses r_s on the other side of the subhalo. In this sense, the scale radius of an NFW profile plays the same role as the truncation radius for a truncated SIS. If the impact parameter is close to the scale radius ($\beta_y \approx r_s/d_L$), then the image trajectory is roughly circular, and it resembles the bottom half of Fig. 2. Unfortunately, the subhalos that are massive enough to deflect the star’s image by several microarcseconds ($M_{\text{vir}} \gtrsim 10^4 M_\odot$) have large scale radii ($r_s \gtrsim 2\text{ pc}$ for $c \lesssim 100$); $\beta_y \approx r_s/d_L$ is a large impact parameter, and the image position changes very slowly as the subhalo moves. Moreover, just as with a truncated SIS lens, the reversal in the image’s motion as the star crosses the scale radius ($\beta \approx r_s/d_L$) is very slow, regardless of the impact parameter β_y .

As in the SIS case, the most promising lensing scenario occurs when the center of the NFW subhalo passes very close to the source. The key difference is that α is nearly constant for $\xi \ll R_t$ if the lens is an SIS, which leads to the semi-circle image trajectory displayed in the top portion of Fig. 2. For an NFW lens with $\xi \ll r_s$, the deflection angle is very small, as shown in the bottom panel of Fig. 4. The NFW density profile leads to a no-win situation: if you decrease the impact parameter β_y in order to enhance the change in the image’s position over a set time period, the magnitude of the deflection decreases. We are forced to conclude that astrometric lensing by subhalos is only detectable if the inner density profile is steeper than $\rho \propto r^{-1}$.

2.3. Generalized density profile

We have seen that astrometric gravitational lensing by subhalos is only detectable if the center of the subhalo passes close to the star’s position during the observational period, during which the subhalo moves about 0.001 pc (for a 5-year observational period). Therefore, only the innermost portion of the subhalo is responsible for the astrometric lensing signature. Unfortunately, very little is known about the intermediate-mass ($10 M_\odot \lesssim M_t \lesssim 10^6 M_\odot$) subhalos that are capable of producing detectable astrometric lensing events. High-resolution N-body simulations can probe the density profiles of only the largest ($M_t \gtrsim 10^8 M_\odot$) subhalos, and even these profiles are unresolved at $r \lesssim 350\text{ pc}$ (Springel et al. 2008; Diemand et al. 2008). For these large subhalos, Diemand et al. (2008) find that $\rho \propto r^{-1.2}$ in the innermost resolved regions, while Springel et al. (2008) see $\rho \propto r^{-(1.2-1.7)}$ at their resolution limit for nine large subhalos, with no indication that the slope had reached a fixed central value. Meanwhile, at the opposite end of the mass spectrum, Diemand et al. (2005) find that the first Earth-mass dark matter microhalos have steeper density profiles with $\rho \propto r^{-(1.5-2.0)}$ at redshift $z = 26$, and higher-resolution simulations indicate that this steep profile extends to within 20 AU of the microhalo center (Ishiyama et al. 2010).

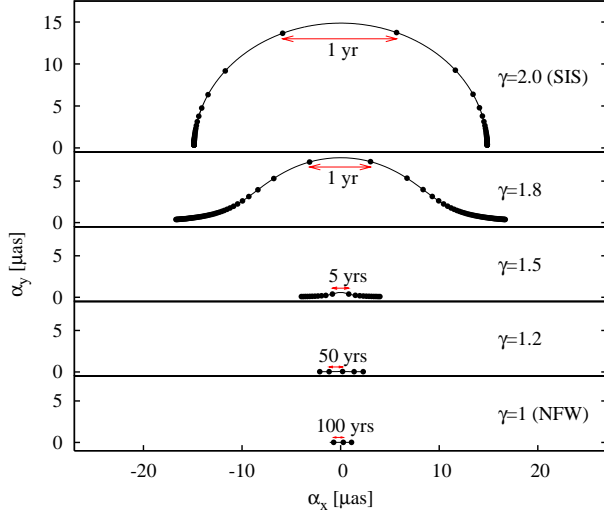


Fig. 4.— The deflection angle generated by a moving lens with $d_S = 5$ kpc, $d_L = 50$ pc and $v_T = 200$ km/s. The virial mass of the lens is $5 \times 10^5 M_\odot$, and its concentration is $R_{\text{vir}}/r_{-2} = 99$. The inner density profile of the lens is given by $\rho \propto r^{-\gamma}$, and the different panels correspond to different values of γ . The impact parameter is 1 arcsecond, and only the portion of the image path corresponding to the time surrounding the moment of closest approach between the image and lens is shown. Note that the image path becomes more linear and the image motion slows down considerably as γ is decreased.

In light of this uncertainty, we consider a generic density profile

$$\rho(r) = \rho_0 \left(\frac{r}{r_0} \right)^{-\gamma} \quad (18)$$

with $1 < \gamma \leq 2$. We assume that a constant-density core, if present, is significantly smaller than our typical impact parameters of 0.001 pc, and we assume that the subhalo does not contain a black hole. Larger cores would decrease the lensing signal while the presence of a black hole would enhance it by adding a point mass and steepening the density profile (Bertone et al. 2005; Ricotti & Gould 2009). If we take this density profile as infinite when calculating the projected surface density Σ , we find that

$$\Sigma(\xi) = \sqrt{\pi} \rho_0 r_0 \frac{\Gamma[0.5(\gamma - 1)]}{\Gamma[0.5\gamma]} \left(\frac{\xi}{r_0} \right)^{1-\gamma}, \quad (19)$$

$$M_{2D}(\xi) = 2\pi^{3/2} (\rho_0 r_0^3) \frac{\Gamma[0.5(\gamma - 1)]}{(3 - \gamma)\Gamma[0.5\gamma]} \left(\frac{\xi}{r_0} \right)^{3-\gamma}, \quad (20)$$

where $\Gamma[x]$ is the Euler gamma function.

Of course, this density profile does not extend to infinity; the subhalo's density profile will be truncated by tidal stripping, and it may also transition to a steeper power law, as in the case of an NFW profile. If the density profile is truncated at $r = R_t$, then the surface density diverges from Eq. (19) as ξ approaches R_t , but for $\xi \ll R_t$, Eqs. (19) and (20) are still good approximations. For instance, if $\gamma = 1.5$ (1.2), $M_{2D}(\xi)$ for a subhalo truncated at R_t is greater than 80% (50%) the value given by Eq. (20) if $\xi \leq 0.1R_t$. We will show in Appendix A that detectable astrometric signatures are only produced if $\xi < 0.03$ pc, and Eq. (20) is accurate to within 20% for subhalos with $\gamma \geq 1.5$, $M_{\text{vir}} < 10^8 M_\odot$, and $R_t \gtrsim 0.1$ pc. Furthermore, the lower bound on R_t is significantly smaller for subhalos with $M_{\text{vir}} \ll 10^8 M_\odot$. We will therefore use Eq. (20) and take $R_t \gtrsim 0.1$ pc as a conservative lower bound, although we note that the resulting deflections may be slightly overes-

timated, especially if $\gamma \lesssim 1.2$. As shown in Fig. 4, however, detecting a subhalo with $\gamma \lesssim 1.2$ is challenging, and we conclude that Eq. (20) is accurate to within $\sim 20\%$ for subhalos of interest.

If a dark matter subhalo with a density profile given by Eq. (18) passes in front of a star, Eq. (1) tells us that

$$\vec{\alpha} = \theta_\alpha \left(\frac{\xi}{r_0} \right)^{2-\gamma} \hat{\xi}, \quad (21)$$

where we have defined

$$\theta_\alpha \equiv 0.88 \mu\text{as} \left(\frac{\Gamma[0.5(\gamma - 1)]}{2(3 - \gamma)\Gamma[0.5\gamma]} \right) \left(1 - \frac{d_L}{d_S} \right) \left(\frac{\text{pc}}{r_0} \right) \left(\frac{\rho_0 r_0^3}{M_\odot} \right). \quad (22)$$

Like θ_E^{SIS} , θ_α depends on the distances to the lens and the source only through the factor $(1 - d_L/d_S)$. We also note that θ_α is related to the Einstein angle θ_E :

$$\theta_\alpha = \theta_E^{\gamma-1} \left(\frac{r_0}{d_L} \right)^{2-\gamma}. \quad (23)$$

We will continue to assume that $\alpha \ll \beta$ so that ξ (see Fig. 1) is approximately equal to $d_L \beta$.

Equation (22) gives the magnitude of the deflection angle in terms of the parameters of the density profile r_0 and ρ_0 , but this is not the most useful description of the subhalo. Instead we characterize the subhalo by either its mass after tidal stripping ($M_t \equiv m_{\text{bd}} M_{\text{vir}}$) or the mass contained within a radius of 0.1 pc from the subhalo center ($M_{0.1\text{pc}}$). Although M_t is a more standard and intuitive description of the subhalo mass, using $M_{0.1\text{pc}}$ offers two advantages. First, $M_{0.1\text{pc}}$ completely determines the deflection angle; without loss of generality, we can set $r_0 = 0.1$ pc, in which case

$$\theta_\alpha = 8.8 \mu\text{as} \left(\frac{\Gamma[0.5(\gamma - 1)]}{2(3 - \gamma)\Gamma[0.5\gamma]} \right) \left(1 - \frac{d_L}{d_S} \right) \left(\frac{3 - \gamma}{4\pi} \right) \left(\frac{M_{0.1\text{pc}}}{M_\odot} \right). \quad (24)$$

Second, $M_{0.1\text{pc}}$ is the portion of the subhalo's mass that is actually probed by astrometric microlensing because truncating the subhalo's density profile at $R_t = 0.1$ pc does not affect its astrometric lensing signature. Therefore, using $M_{0.1\text{pc}}$ to characterize the subhalo's mass allows us to consider subhalos that are more compact than standard virialized subhalos and makes it easy to apply our results to more exotic forms of dark matter substructure.

To relate θ_α to the virial mass of the subhalo, we have to specify the full density profile. If $\gamma = 2.0$, we will assume that the subhalo is a truncated SIS so that Eq. (18) holds out to the truncation radius of the subhalo. In this case, Eq. (23) tells us that $\theta_\alpha = \theta_E^{\text{SIS}}$, and we can use Eq. (10) to evaluate θ_α . If $\gamma \neq 2$, we will assume that the subhalo's full density profile prior to any tidal stripping was

$$\rho(r) = \frac{\rho_0}{\left(\frac{r}{r_0} \right)^\gamma \left(1 + \frac{r}{r_0} \right)^{3-\gamma}}, \quad (25)$$

which reduces to Eq. (18) for $r \ll r_0$. In this case, the virial mass does not uniquely determine θ_α , and we also have to specify the subhalo's concentration. We define the concentration as $c \equiv R_{\text{vir}}/r_{-2}$, where r_{-2} is the radius at which $d \ln \rho / d \ln r = -2$. For the profile given by Eq. (25),

$r_{-2} = (2 - \gamma)r_0$. It follows that

$$r_0 = 27 \text{ pc} \left(\frac{1}{2 - \gamma} \right) \left(\frac{94}{c} \right) \left(\frac{M_{\text{vir}}}{10^6 M_{\odot}} \right)^{1/3} \left(\frac{\bar{\rho}_{\text{vir}}(z_v)}{4.6 M_{\oplus} \text{ pc}^{-3}} \right)^{-1/3}. \quad (26)$$

We see that r_0 is larger than 5 pc for the subhalos we consider ($M_{\text{vir}} \geq 10^4 M_{\odot}$ and $\gamma \geq 1.2$), and we expect that local subhalos will be stripped to much smaller radii by encounters with stars.

We can now derive how θ_{α} depends on the subhalo's virial mass and concentration. Recall from Eq. (22) that $\theta_{\alpha} \propto \rho_0 r_0^2$. For the profile given by Eq. (25), this factor is related to the subhalo's concentration and virial mass through

$$\left(\frac{\text{pc}}{r_0} \right) \left(\frac{\rho_0 r_0^3}{M_{\odot}} \right) = 810 \left(\frac{c}{94} \right) \left(\frac{M_{\text{vir}}}{10^6 M_{\odot}} \right)^{2/3} \left(\frac{\bar{\rho}_{\text{vir}}(z_v)}{4.6 M_{\oplus} \text{ pc}^{-3}} \right)^{1/3} \times \left[\frac{3.57(-1)^{\gamma}(\gamma - 2)}{B[c(\gamma - 2); 3 - \gamma, \gamma - 2]} \right], \quad (27)$$

where $B[z; a, b]$ is the incomplete Beta function. In Appendix B.2, we use the findings of the Aquarius simulation (Springel et al. 2008) to derive a relationship between the concentration of local subhalos and their virial mass:

$$c = 94 \left(\frac{M_{\text{vir}}}{10^6 M_{\odot}} \right)^{-0.067}, \quad (28)$$

and we use this relation to determine the subhalo concentration throughout this investigation.

Figure 4 shows the paths taken by the star's image as the center of a subhalo passes 1 arcsec below the star's position for several values of γ . In this figure, $d_L = 50$ pc, $d_S = 5$ kpc, $v_T = 200$ km/s, and the subhalo lens has a virial mass of $5 \times 10^5 M_{\odot}$. We see that the image path depends very strongly on γ . If $\gamma \approx 1$, the motion is nearly linear, and the image moves very little and very slowly. As γ increases, an arc appears in the image path; there is now sufficient mass enclosed in the inner arcsecond to cause an observable vertical deflection when the subhalo passes beneath the star. Increasing γ also increases the motion of the image in a given time period, and the acceleration of the image as the subhalo approaches the point of closest approach becomes apparent. As the subhalo center passes from the left to the right of star, the star's image will jump from right to left; since the image moves very slowly in the years before and after the crossing of the subhalo, this shift in the image's position offers the best hope for detection.

3. OBSERVING STRATEGY

The image motions shown in Fig. 4 suggest a simple detection strategy for subhalo lensing, illustrated in Fig. 5. A typical high-precision astrometric search program operates for up to 10 years. We start with an initial few-year calibration period, during which we assume that the star is relatively far from the lens. During this calibration period we 1) measure the star's intrinsic proper motion, parallax, and starting position and 2) search for binary stars or other false positives. Stars that show significant acceleration during the calibration period probably have binary companions, and we reject them from the rest of the search. We follow the calibration period with a several-year detection run, when we essentially wait for a subhalo lens to come close to one of our target stars and induce significant lensing.

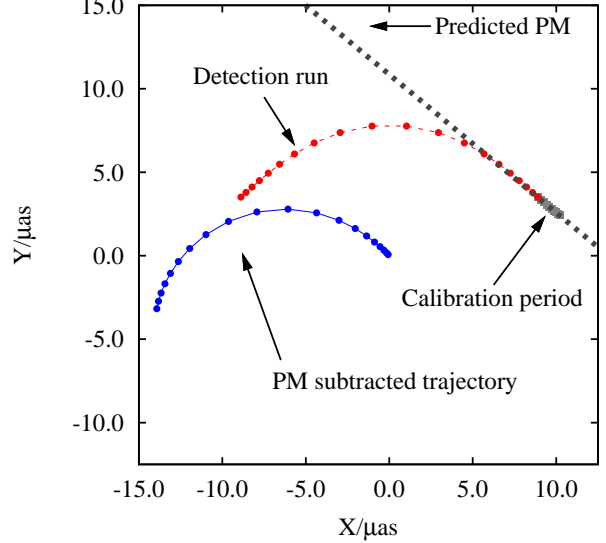


FIG. 5.— The subhalo lens detection scheme. The dashed line shows the trajectory of an image induced over 6 years by a subhalo lens with the same properties as in Fig. 4 and $\gamma = 1.8$. The image motion during the calibration period and the detection run are labeled. The dotted line shows the direction of the proper motion fitted during the calibration period, and the difference between the measured trajectory and the proper motion prediction is shown by the solid curve. For clarity, the intrinsic proper motion and parallax of the source are not shown.

The timescale of the calibration period is important, as it needs to be long enough both to detect binary systems and to obtain a robust parallax and proper motion measurement. Increasing the calibration period length improves the predicted-position accuracy, but it also takes time away from the detection run, reducing the probability of observing a lensing event. The calibration period must be at least one year long to obtain a secure parallax, and we suggest two years as a sensible length to ensure an accurate parallax and proper motion measurement. The length of the detection run is then set by the duration of the high-precision astrometric campaign. In this analysis, we assume a four-year detection run, implying a total of six years of observations, which is close to the expected mission lengths of Gaia and SIM and a reasonable length for long-term ground-based surveys. We leave a full discussion of the optimal observing strategy to future work, as the details of the observing scenario will depend on both the particular astrometric technique and the time available for the observations.

For the purposes of this paper, we adopt a simple measurement of the astrometric signal from a lensing event:

$$S = \sqrt{\sum_{i=1}^{N_{\text{epochs}}} (Xm_i - Xp_i)^2 + (Ym_i - Yp_i)^2}, \quad (29)$$

where Xm_i and Ym_i give the 2D measured position of the star at each epoch, and Xp_i and Yp_i give the 2D position of the star predicted from the proper motion, parallax and position determined during the calibration period. This calculation (following Gaudi & Bloom 2005) essentially measures the total displacement of the star from its expected position over the course of the measurements. The signal-to-noise ratio (S/N) is simply S divided by the astrometric uncertainty per 1D datapoint (σ); σ includes contributions from the instrument's intrinsic uncertainty per datapoint as well as uncertainty in the star's proper motion, parallax and position.

The uncertainty in the star’s predicted position grows in time due to the proper-motion uncertainty, and the parallax uncertainty’s effect on the 2D measurements varies in direction and magnitude across the sky.

This calculation gives a conservative estimate of the S/N of a possible lensing detection. The displacements induced by lensing are all in approximately the same direction, however, and the effective S/N would likely be improved by fitting a model to the data that accounts for these correlations. We leave such enhancements for future work.

3.1. False positive removal

In addition to simply detecting a subhalo lensing signal, we must also distinguish it from other astrometric signals. Subhalo lensing signals take place over months, do not repeat, occur without a visible lensing source, and have a near-unique trajectory. The relatively short event timescales ensure that our measurements are only sensitive matter structures on the spatial scales we consider here. The events’ other properties can be used to remove false positives, such as those generated by stellar microlensing and motion in binary systems.

Astrometric microlensing by a passing point-like lens moves the image centroid along an elliptical path that becomes more circular as the impact parameter increases (Walker 1995; Paczynski 1995, 1998; Miralda-Escude 1996; Gould 2000). The image path can become more complicated if the lens has a small finite extent and is opaque (Takahashi 2003; Lee et al. 2010). In all cases, however, the image completes its orbit on observable timescales, quickly approaching its true position as the compact object moves further away. We saw in the previous section that subhalos produce a radically different lensing signature; after the passage of the subhalo center, the image moves very slowly and does not approach its true position until the edge of the subhalo passes by the star many decades later. Lensing by subhalos is therefore readily distinguishable from lensing by compact objects.

The astrometric signal of a stellar binary is easily distinguished from subhalo lensing signals in most cases simply because the binary system produces a repeating signal. Almost all long-period systems that do not produce repeating signals in our dataset will be removed by our requirement that the star does not accelerate during the calibration period. Furthermore, roughly circular binary systems induce a very different astrometric signal from subhalo lenses.

Rare highly eccentric systems with periods much longer than our observation length (or even very close unbound stellar encounters) can produce a short-timescale astrometric signal during periastron, with little signal throughout much of rest of the orbit. The trajectory is similar to a lensing signature (with an additional very large radial velocity signal). However, simple simulations of such systems show that no Keplerian orbit (of any eccentricity < 0.999) that produces a lensing-like signal can avoid producing detectable acceleration both during the calibration period and after the putative lensing event.

3.2. Final subhalo lens confirmation

The ultimate test of a candidate subhalo is a *prediction* of lensing. We will show in the next section that detectable dark matter subhalos are probably within 100 pc of our location; while it is possible to detect a more distant subhalo, the subhalo would have to be massive ($M_{\text{vir}} \gtrsim 10^6 M_{\odot}$), and we expect such objects to rarely pass between us and a target star.

Detectable dark matter subhalos are therefore likely to have proper motions greater than half an arcsecond per year, and they will astrometrically affect all stars within several arcseconds of the subhalo center. If a halo is detected, its path can be predicted (albeit initially at low precision), and a catalog prepared of stars that are likely to be affected by lensing over the next few years. Intensive astrometric monitoring of faint stars in the field could then provide a fairly rapid confirmation of the existence of the subhalo lens.

4. CROSS SECTIONS FOR ASTROMETRIC LENSING BY SUBHALOS

4.1. Signal Calculations

As described in Section 3, we calculate the lensing signal by taking the square root of the sum of the squared differences between the star’s position on the sky and the position predicted by the proper motion and parallax measured during the calibration period [Eq. (29)]. At each epoch, the difference between the measured image position and the predicted position is proportional to the deflection angle $\vec{\alpha}$. This linearity implies that we may use any vector $\vec{\eta}$ that is proportional to $\vec{\alpha}$ to calculate the signal; we just have to multiply the resulting signal by α/η to obtain the physical signal that would be measured during a lensing event. We use this technique to separate the signal’s dependence on the geometry of the lensing scenario from its dependence on the properties of the lens. As we describe in detail below, we can then calculate the geometrical signal once and then use that result to determine the signal for any lens.

Following our convention, we work in a coordinate system where the subhalo’s transverse velocity \vec{v}_T lies along the x -axis. In this case, β_y is the fixed impact parameter, and $\beta_{x,0}$ specifies the initial position of the lens. It is useful to define

$$\varphi \equiv \frac{d_L \beta_{x,0}}{v_T t_{\text{obs}}} \quad \text{and} \quad \tilde{\beta} \equiv \frac{d_L \beta_y}{v_T t_{\text{obs}}}, \quad (30)$$

where $\beta_{x,0}$ and β_y are in radians, and t_{obs} is the length of the observation (not including the calibration period). If we define $\Delta\beta$ to be the angular distance, in radians, traversed by the lens during the observational period, we can easily interpret φ and $\tilde{\beta}$. The normalized impact parameter $\tilde{\beta} = \beta_y/\Delta\beta$, while the phase $\varphi = \beta_{x,0}/\Delta\beta$ specifies the location of the point of closest approach to the star along the subhalo’s path. Since we are only interested in cases where the subhalo center passes by the star during the observational period, we constrain $0 < \varphi < 1$. With these definitions Eq. (21) may be rewritten as

$$\vec{\alpha} = \theta_{\alpha} \left(\frac{v_T t_{\text{obs}}}{r_0} \right)^{2-\gamma} \vec{\eta}(\varphi, \tilde{\beta}, t/t_{\text{obs}}, \gamma), \quad (31)$$

which allows us to separate the geometry of the lens-star system (i.e. φ and $\tilde{\beta}$) from all of the lens characteristics apart from γ . From Eq. (21), we see that

$$\vec{\eta} = \tilde{\beta} \left(\frac{\xi}{v_T t_{\text{obs}}} \right)^{2-\gamma} = \left[\sqrt{\left(\varphi - \frac{t}{t_{\text{obs}}} \right)^2 + \tilde{\beta}^2} \right]^{1-\gamma} \left[\left(\varphi - \frac{t}{t_{\text{obs}}} \right) \hat{x} + \tilde{\beta} \hat{y} \right]. \quad (32)$$

We use $\vec{\eta}$ to calculate the signal of a lensing event. This is advantageous because the resulting signal is independent of θ_{α} , d_L , and v_T ; we call this signal S_g (for “geometrical signal”) because it depends only on φ , $\tilde{\beta}$, and γ . The calculation

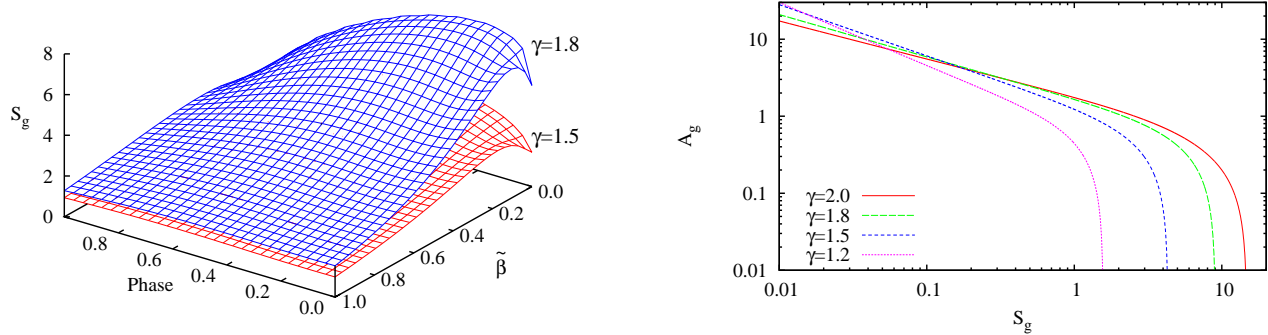


FIG. 6.— *Left*: The signal S_g as a function of phase (φ) and impact parameter $\tilde{\beta} \equiv \beta_y/\Delta\beta$ for a two-year calibration period and a four-year detection run. Note the decrease in signal toward larger phases, where the image only partially traverses its lensing path during the observational period. The decrease in S_g at the smallest phases and impact parameters corresponds to lenses that start to produce large image motion during the calibration period, which is then partially subtracted out by the proper motion removal during the detection run. At larger values of $\tilde{\beta}$ the apparent motions are still relatively large (see Fig. 3, for instance), but these motions are difficult to distinguish from the star’s proper motion, leading to the decrease in S_g . *Right*: The area A_g in the $\varphi - \tilde{\beta}$ plane that produces a geometrical signal that is larger than a given value for S_g for a variety of γ values. Note that the normalized area goes to zero at a value of S_g that is dependent on γ . For S_g values much smaller than this cut-off, A_g is proportional to $(S_g)^p$, where the index p depends on γ .

of S_g takes into account the subtraction of the proper motion and parallax measured during the calibration period, including any apparent motion generated by lensing, as shown in Fig. 5. Figure 6 shows $S_g(\varphi, \tilde{\beta})$ for $\gamma = 1.5$ and $\gamma = 1.8$. We see that S_g decreases with increasing impact parameter $\tilde{\beta}$ and increases with increasing γ , which is not surprising given the image paths shown in Fig. 4. We also see a preference for geometries in which the subhalo passes by the star earlier in the observational period; the signal is enhanced because there are more epochs after the shift in the star’s position when the subhalo center passes the star.

To relate the physical signal S to the geometrical signal S_g we use

$$S = \theta_\alpha \left(\frac{v_T t_{\text{obs}}}{r_0} \right)^{2-\gamma} S_g. \quad (34)$$

This relation completes the procedure for determining if a star is detectably lensed by a given subhalo. Given a specific lens and a minimal detectable value for the signal S_{min} , Eq. (34) may be inverted to obtain the corresponding minimal value for S_g . We then determine the area A_g of the region in the $\varphi - \tilde{\beta}$ plane (with $0 < \varphi < 1$ and $\tilde{\beta} > 0$) that produces a geometrical signal that exceeds this minimal value for S_g . Finally, we convert A_g to a physical area on the sky that gives $S > S_{\text{min}}$, and we call this area the cross-section $A(S_{\text{min}})$; in square radians we have

$$A(S_{\text{min}}) = 2 \left(\frac{v_T t_{\text{obs}}}{d_L} \right)^2 A_g(S_g). \quad (35)$$

The factor of 2 accounts for the fact that the stars both above ($\tilde{\beta} > 0$) and below ($\tilde{\beta} < 0$) the lens are equally deflected, and the two factors of $(v_T t_{\text{obs}}/d_L)$ follow from the definitions of φ and $\tilde{\beta}$ [see Eq. (30)].

The geometrical area functions $A_g(S_g)$ are shown in the right panel of Fig. 6 for several value of γ . As indicated by the $S_g(\varphi, \tilde{\beta})$ surfaces shown in the left panel of Fig. 6, the area A_g that produces a geometrical signal larger than a specific S_g value depends strongly on γ and decreases rapidly with increasing S_g . The left panel also shows that S_g does not go to

infinity as the impact parameter $\tilde{\beta}$ goes to zero. Consequently, there is a maximal value of S_g that is obtainable for each value of γ . At this value of S_g , the area A_g goes to zero, as shown in the right panel of Fig. 6. This maximal obtainable value of S_g implies that there is a minimum subhalo mass that is capable of generating a detectable signal, as we will see in the next subsection. For values of S_g that are smaller than half of the maximal possible S_g value, $A_g \propto (S_g)^p$, as shown in the right panel of Fig. 6. For the four γ values we tested, we found that $p = -1/\gamma$. This simple power-law behavior will be shared by the physical lensing cross sections.

4.2. Properties of the Lensing Cross Sections

The basic shape of the lensing cross sections can be deduced from the left panel of Fig. 6. This figure shows that S_g does not depend strongly on the phase φ when S_g is smaller than the maximum obtainable geometrical signal. For S_{min} values that correspond to these values of S_g , the lensing cross sections are rectangular. The width of the rectangle is given by the change in the lens position during the observational period ($\Delta\beta$) because we only consider lensing scenarios with $0 < \varphi < 1$. The length of the rectangle is two times the maximum impact parameter that a star may have and still be detectably lensed. The impact parameters that lie within the lensing cross section are therefore bounded by $|\beta_y| \lesssim A(S_{\text{min}})/(2\Delta\beta)$. For a lens at a distance of 50 pc with $v_T = 200$ km/s, Eq. (2) tells us that $\Delta\beta \approx 3$ arcseconds for a four-year observational period, so the maximum impact parameter that produces a lensing signal $S > S_{\text{min}}$ is $\beta_y \approx A(S_{\text{min}})/(6 \text{ arcsec})$.

Figure 7 shows how the lensing cross section depends on the mass of the subhalo for three values of S_{min} : $5 \mu\text{as}$, $20 \mu\text{as}$, and $50 \mu\text{as}$. We characterize the mass of the subhalo in two ways, as discussed in Section 2.3. In the top row, we show the cross section as a function of the mass enclosed in the inner 0.1 pc of the subhalo ($M_{0.1\text{pc}}$). Recall that truncating the subhalo density profile at a radius of 0.1 pc does not significantly alter the lensing signal, which implies that $M_{0.1\text{pc}}$ directly determines the lensing signature. In the bottom row, we show how the lensing cross section depends subhalo’s virial mass.

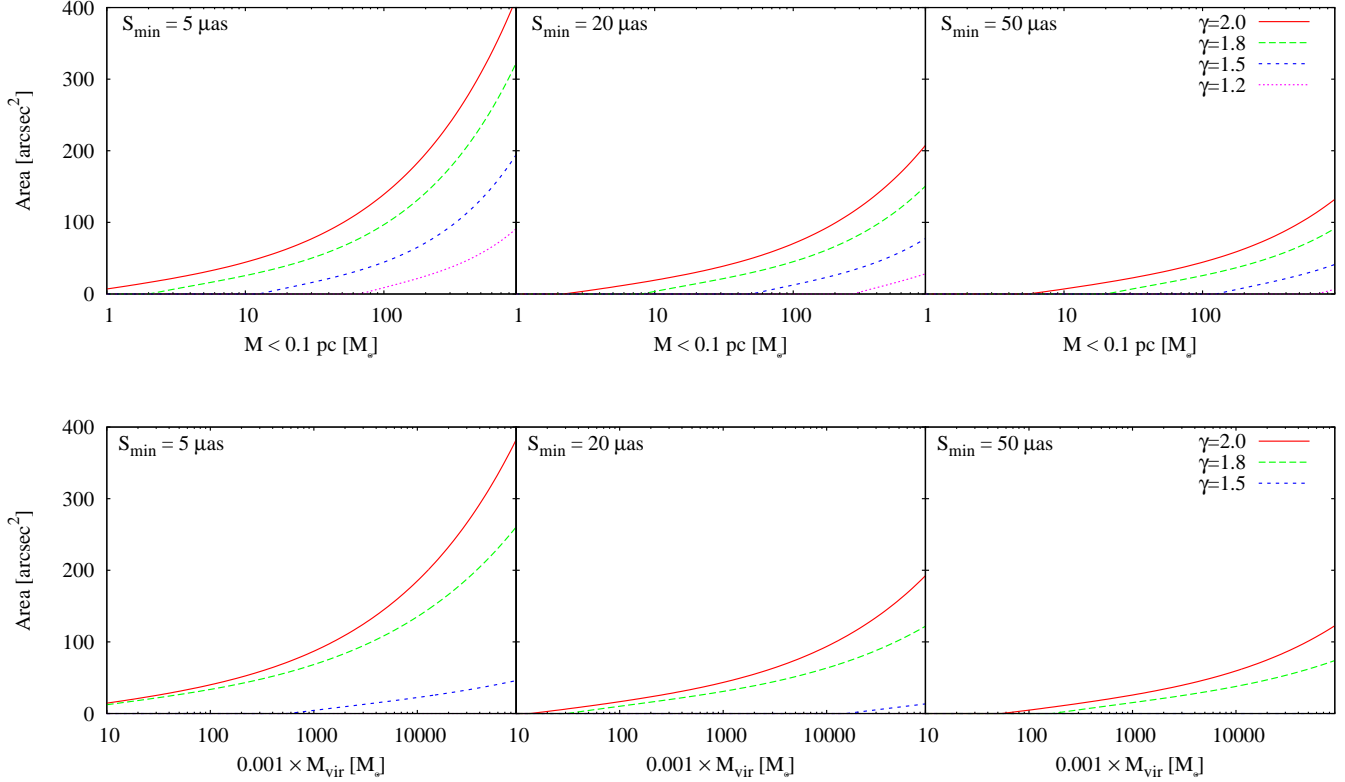


Fig. 7.— The area around a subhalo that will produce an astrometric signal greater than S_{\min} as a function of subhalo mass, with $d_L = 50$ pc, $d_S = 5$ kpc, and $v_T = 200$ km/s. *Top*: The mass of the subhalo is defined as the mass contained within a radius of 0.1 pc from its center. Truncating the subhalo density profile at a radius of 0.1 pc does not affect its lensing signature. *Bottom*: The mass of the subhalo is defined as 0.1% of its virial mass. The area curves for $\gamma = 1.2$ are not shown because the subhalo must have $M_{\text{vir}} > 10^8 M_\odot$ to generate a signal of at least $5 \mu\text{as}$ if $\gamma = 1.2$.

We assume that 99.9% of the subhalo’s virial mass has been lost due to tidal stripping and take $0.001M_{\text{vir}}$ as the present-day mass of the subhalo.

From Fig. 7, we can see how the inner slope of the density profile determines the strength of the lens signature; in all cases, the lensing cross section decreases sharply with decreasing γ . The dependence on γ is stronger when the virial mass is used to define the mass of subhalo because a shallower density profile requires a larger virial mass to get the same mass within a given radius. The bottom row of Fig. 7 indicates that subhalos with $\gamma < 1.5$ are not capable of generating easily detectable astrometric lensing signatures, and subhalos with $\gamma = 1.5$ are only detectable if a star passes within a couple of arcseconds of the subhalo center. The situation is far more promising for subhalos with $\gamma \gtrsim 1.8$; in this case, an intermediate-mass subhalo could produce a signal of up to $50 \mu\text{as}$ if a star passes within 10 arcseconds of the subhalo center. Moreover, we see that small subhalos ($M_t \lesssim 1000 M_\odot$) are so concentrated that decreasing the inner slope of the density profile from $\gamma = 2$ to $\gamma = 1.8$ does not significantly change the astrometric lensing signal. Finally, the top row of Fig. 7 shows that if the inner regions of the subhalos are denser than predicted by their virial masses, subhalos with shallower density profiles are capable of producing detectable signals.

For S_{\min} values that correspond to geometrical signals well below the maximal possible value for S_g (the value of S_g at which $A_g = 0$), the cross section has a simple dependence on S_{\min} : A is proportional to $(S_{\min})^p$, with $p = -1/\gamma$ for the four values of γ we consider. This simple power law is di-

rectly inherited from the geometrical area functions $A_g(S_g)$ discussed in the previous section and shown in the right panel of Fig. 6. Consequently, the power index p is independent of d_L , d_S , v_T , and subhalo mass, and it is even independent of whether $M_{0.1\text{pc}}$ or M_{vir} is used to characterize the subhalo mass. As S_{\min} increases toward the maximal possible value, the cross section decreases faster than $(S_{\min})^p$ and rapidly goes to zero when the maximal possible value for S_{\min} is reached.

4.3. Lensing Event Rates

The lensing cross sections computed in the previous sections may be combined with a subhalo number density to yield a probability that any given star on the sky will be detectably lensed during the observational period. In this section, we will compute these probabilities using three candidate subhalo number densities. The first two calculations will assume that all the subhalos have the same mass; we will assume that a fraction f of the local dark matter halo is composed of subhalos with mass M and radii of $R = 0.1$ pc, and then we will assume that the local dark matter halo was once in subhalos with virial mass M_{vir} . We take the local dark matter density ρ_{dm} to be 0.4 GeV cm^{-3} , which implies that there is $3.5 \times 10^8 M_\odot$ of dark matter within 2 kpc. Finally, we will use a subhalo mass function derived from the Aquarius simulations (Springel et al. 2008). Throughout this section, we will use $v_T = 200$ km/s and $t_{\text{obs}} = 4$ years.

We compute the lensing probabilities by summing the individual cross sections for all subhalos with $d_L < d_S$ for some fixed value of d_S . We choose d_S to be small enough that we may neglect the spatial variation in the subhalo number den-

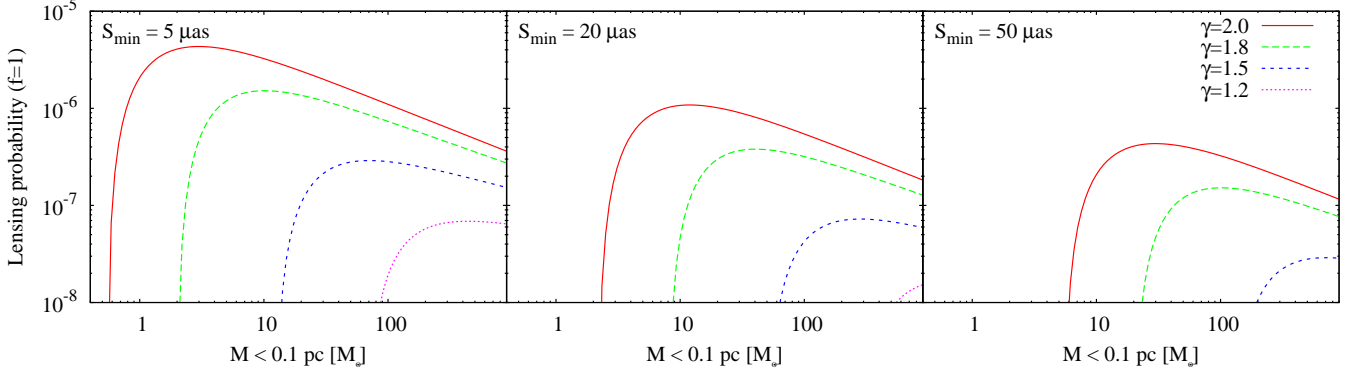


FIG. 8.— The probability that a star is detectably lensed, with signal $S > S_{\min}$, if all subhalos have the same mass M within the inner 0.1 pc. The local number density of the subhalos is $f\rho_{\text{dm}}/M$, where ρ_{dm} is the local dark matter density, and f is the fraction of the dark matter contained within 0.1 pc of a subhalo center. The lensing probability is proportional to f , and $f = 1$ is shown here to illustrate the maximal possible lensing probability.

sity within this sphere, and we assume that the subhalos are isotropically distributed. From Eq. (35), we see that the lensing cross section for an individual halo is $A \propto d_L^{-2} A_g$, and A_g depends on d_L only through the $(1 - d_L/d_S)$ factor in θ_α . It follows that the total cross section is

$$A_{\text{tot}} = 8\pi (v_{\text{T}} t_{\text{obs}})^2 d_S n_{\text{sub}}(M) \times \int_0^1 A_g \left[\frac{S_{\min}}{\theta_\alpha(x = d_L/d_S)} \left(\frac{r_0}{v_{\text{T}} t_{\text{obs}}} \right)^{2-\gamma} \right] dx, \quad (36)$$

where $n_{\text{sub}}(M)$ is the number density of subhalos with mass M . Although d_S will typically vary from less than 1 kpc to 5 kpc for stars in a high-precision astrometric survey, we simplify the calculation by assuming that all the monitored stars are 2 kpc from us. Since A_{tot} increases linearly with d_S , taking $d_S = 2$ kpc effectively averages over stars that are uniformly distributed over $1 \text{ kpc} < d_S < 3 \text{ kpc}$.

We will see that the resulting total cross section A_{tot} is much smaller than the total area of the sky A_{sky} . It is therefore highly unlikely that the cross section for lensing by one subhalo will overlap with the cross section associated with a different subhalo, and we may consider A_{tot} to be the total area on the sky in which a star would be detectably lensed. Furthermore, since the individual subhalo lensing cross sections are less than 0.1 square arcminute (see Fig. 7), the probability of having multiple stars within the cross section of a particular subhalo is low enough that we may consider each star to be an independent sample of the sky. In this case, we may interpret the fraction $A_{\text{tot}}/A_{\text{sky}}$ as the probability that any single star is detectably lensed by a subhalo. A subhalo in the Galactic plane is more likely to be detected than a subhalo near the Galactic pole due to the higher density of target stars in the plane, but, since the subhalos are isotropically distributed and can only lens one star apiece, the average lensing probability ($A_{\text{tot}}/A_{\text{sky}}$) is individually applicable to each star in the sky.

4.3.1. Event Rates: Mono-mass subhalos

We first consider cases where all the subhalos have the same mass $M_{0.1\text{pc}}$ within a radius of 0.1 pc. The local subhalo number density is then $n_{\text{sub}} = f\rho_{\text{dm}}/M_{0.1\text{pc}}$, where f is the fraction of the dark matter that is contained in the inner 0.1 pc of the subhalos; $f < 1$ could mean that there is a smooth component of the local dark matter distribution, or it could mean that the subhalos' radii are larger than 0.1 pc and their actual masses are $M_{0.1\text{pc}}/f$. In Fig. 8, we show the lensing probability with $f = 1$ for three values of S_{\min} : $5 \mu\text{as}$, $20 \mu\text{as}$, and $50 \mu\text{as}$. We

see that the lensing probability is highest for each value of γ if the subhalo mass is just slightly larger than the minimum mass required to generate a sufficiently large signal. Although more massive subhalos have larger cross sections, as shown in Fig. 7, the dependence of A on $M_{0.1\text{pc}}$ is not steep enough to compensate for the diminishing number density of subhalos as $M_{0.1\text{pc}}$ increases.

If we instead assume that all of the local dark matter was originally in subhalos with virial mass M_{vir} and that the central regions of these subhalos survive to the present day, then the subhalo number density is $n_{\text{sub}} = \rho_{\text{dm}}/M_{\text{vir}}$. As in the previous case, the $(1/M_{\text{vir}})$ factor in n_{sub} implies that the lensing probability will peak near smallest value of M_{vir} that is capable of generating a signal. For $S_{\min} = 5\mu\text{as}$, the lensing probability peaks at $M_{\text{vir}} \approx 10^4 M_\odot$ for $\gamma = 2$ and $\gamma = 1.8$, and $M_{\text{vir}} \approx 10^{6.5} M_\odot$ for $\gamma = 1.5$, as predicted by Fig. 7. Since the cross section for these smaller subhalos does not change much between $\gamma = 1.8$ and $\gamma = 2.0$, the lensing probabilities for these two cases are very similar and they peak at probabilities of 5×10^{-10} and 7×10^{-10} , respectively. The $\gamma = 1.5$ case peaks a far lower probability of 1×10^{-12} . It is not surprising that these numbers are about four orders of magnitude lower than the peak probabilities in Fig. 8; from Fig. 7, we see that $A(M_{0.1\text{pc}}) \sim A(M_{\text{vir}})$ for $M_{0.1\text{pc}} \sim 10^{-4} M_{\text{vir}}$ and $\gamma = 2$, so by setting $n_{\text{sub}} = \rho_{\text{dm}}/M_{\text{vir}}$, we are effectively setting $f \sim 10^{-4}$ in Fig. 8.

When we assume that all the subhalos have the same mass, then A_{tot} has the same simple dependence on S_{\min} as A ; for S_g values that are small compared to the maximum accessible value, A_{tot} is proportional to $(S_{\min})^p$, with $p = -1/\gamma$ as in Section 4.2. If we instead consider a subhalo mass function and integrate over subhalo masses, the dependence of A_{tot} on S_{\min} changes because there is no longer a single value of S_{\min} that corresponds to the value of S_g at which $A_g = 0$.

4.3.2. Event Rates: subhalo mass function

To evaluate the lensing probability with a range of subhalo masses, we will use the local subhalo mass function derived in Appendix B.1 from the results of the Aquarius simulations (Springel et al. 2008):

$$\frac{dn_{\text{sub}}}{dM_{\text{vir}}} = 2 \times 10^{-5} \left(\frac{M_{\text{vir}}}{M_\odot} \right)^{-1.9}. \quad (37)$$

As described in Appendix B.1, this subhalo mass function is applicable within a few kpc of the Sun, and we have assumed

that the subhalos in this region lose 99% of their virial mass due to tidal stripping by the smooth component of the dark matter halo and other subhalos (stars are not included). We evaluate A_{tot} by replacing n_{sub} in Eq. (36) with $dn_{\text{sub}}/dM_{\text{vir}}$ and integrating over M_{vir} from M_{min} to M_{max} . For each value of γ and S_{min} , there is a minimal value of M_{vir} needed to make A_g nonzero; this minimal virial mass is always larger than $10 M_{\odot}$, so we set $M_{\text{min}} = 10 M_{\odot}$. We choose M_{max} such that the expectation value for the number of subhalos with $M_{\text{vir}} \geq M_{\text{max}}$ within 2 kpc is greater than one; from Eq. (37), we have $M_{\text{max}} = 3 \times 10^6 M_{\odot}$. Extending the integral to larger values of M_{vir} changes the meaning of A_{tot} ; it is no longer a sum of cross sections for the subhalos expected to be within 2 kpc. Instead, A_{tot} would also include the cross sections for subhalos that we do not expect to find within 2 kpc, multiplied by the probability that such a halo is in this volume.

The value of M_{max} determines the shape of the $A_{\text{tot}}(S_{\text{min}})$ function because it determines the value of S_{min} at which A_{tot} goes to zero. If $S_g(S_{\text{min}}, M_{\text{max}})$ is greater than the maximum reachable value for S_g , then no subhalo with $M_{\text{vir}} < M_{\text{max}}$ can generate a signal and $A_{\text{tot}} = 0$. For $\gamma = 1.2, 1.5, 1.8,$ and 2.0 , this maximum value for S_{min} is $0.46, 10, 250,$ and $750 \mu\text{as}$, respectively. If S_{min} is much less than these upper limits, then $A_{\text{tot}}(S_{\text{min}})$ is roughly a power law, and the lensing probability is approximately

$$\left. \frac{A_{\text{tot}}}{A_{\text{sky}}} \right|_{\gamma=1.8} = 8.7 \times 10^{-12} \left(\frac{S_{\text{min}}}{5 \mu\text{as}} \right)^{-1.74} \quad \text{for } S_{\text{min}} < 80 \mu\text{as}, \quad (38)$$

$$\left. \frac{A_{\text{tot}}}{A_{\text{sky}}} \right|_{\gamma=2.0} = 1.3 \times 10^{-11} \left(\frac{S_{\text{min}}}{5 \mu\text{as}} \right)^{-1.44} \quad \text{for } S_{\text{min}} < 200 \mu\text{as}. \quad (39)$$

For larger values of S_{min} , $A_{\text{tot}}(S_{\text{min}})$ decreases faster than these expressions and quickly goes to zero at the values listed above. If $\gamma = 1.5$, then $A_{\text{tot}}/A_{\text{sky}} = 1.4 \times 10^{-12}$ for $S_{\text{min}} = 1 \mu\text{as}$, and there is no power-law behavior between $S_{\text{min}} = 1 \mu\text{as}$ and the zero point at $S_{\text{min}} = 10 \mu\text{as}$.

Including the probabilities that larger subhalos are present within 2 kpc of our location does not significantly affect the total lensing cross section. If we set $M_{\text{max}} = 10^{10} M_{\odot}$, then the dependence of A_{tot} on S_{min} is slightly shallower than the power laws given in Eqs. (38) and (39), but the differences are not large. For $S_{\text{min}} \lesssim 20 \mu\text{as}$, including subhalos with $3 \times 10^6 M_{\odot} < M_{\text{vir}} < 10^{10} M_{\odot}$ increases the lensing probability by less than 20%. At the largest S_{min} values described by Eqs. (38) and (39), extending the integral to these larger subhalo masses increases A_{tot} by a factor of three. The inclusion of larger subhalos has a more pronounced impact on the value of A_{tot} for $S_{\text{min}} \geq 0.46, 10, 250,$ and $750 \mu\text{as}$ for $\gamma = 1.2, 1.5, 1.8,$ and 2.0 , respectively. The larger value of M_{max} implies that the total cross section does not go to zero at these values of S_{min} as it did when we set $M_{\text{max}} = 3 \times 10^6 M_{\odot}$. This is not an important change, however, because the lensing probability is less than 10^{-13} for these large values of S_{min} . Moreover, even if it were possible to monitor far more than 10^{13} target stars, lensing events would only be observed if a subhalo with $M_{\text{vir}} > 3 \times 10^6 M_{\odot}$ lies between us and the target stars.

5. DETECTION PROSPECTS

As discussed in the introduction, it is only recently that astrometric capabilities have advanced to levels where the detection of subhalo lenses becomes possible. In this section we use the results derived above to evaluate current and future astrometric subhalo search techniques. We consider two

scenarios: 1) a large-area search for subhalo lenses and 2) a confirmation of a subhalo suspected on the basis of other detection methods.

5.1. Achievable S_{min}

We start by evaluating the achievable S_{min} for an astrometric survey. For a particular astrometric observing strategy, both the number of epochs and the astrometric precision affect S_{min} . For the purposes of this discussion we calculate the best S_{min} for each technique using the six-year observation setup described in Section 3. We include the single epoch instrumental uncertainty, as well as a detailed Monte Carlo simulation of the extra per-epoch uncertainties introduced by the measurement and subtraction of the target star's calibration-period position, proper motion and parallax. We marginalize over a wide range of possible parallaxes and proper motions, as well as the full range of possible sky positions.

For a particular observational setup, the simulations produce a scaling factor between the instrumental astrometric uncertainty per epoch (σ_{inst}) and the final total uncertainty per datapoint (σ) used to calculate S/N. For the observational setup described in Section 3, $\sigma = 1.47\sigma_{\text{inst}}$. For a typical S/N = 3 detection, an instrument's S_{min} is then $4.4\sigma_{\text{inst}}$. We note that the summed nature of S_{min} means that astrometric displacements smaller than σ_{inst} are indeed detectable in this scheme.

5.2. Large-Area Surveys

A practical all-sky search for subhalo lenses requires enough stars that the lensing probabilities described above lead to a significant probability of detection. For example, following the left panel of Fig. 8, if all subhalo lenses are singular isothermal spheres and have a $M_{0.1\text{pc}}$ of $2 M_{\odot}$, and our survey is capable of detecting $S_{\text{min}}=5 \mu\text{as}$, we need to survey $\sim 5f^{-1} \times 10^5$ stars to have a good chance of detecting a subhalo lens, where f is the fraction of local dark matter that is contained within 0.1 pc of a subhalo center. Alternately, at an S_{min} of $50 \mu\text{as}$ we need to survey $\sim 3f^{-1} \times 10^6$ stars.

Ground-based all-sky surveys are currently limited to milliarcsecond precisions at best (e.g., Ivezić et al. 2008), so we do not consider them further here. The Gaia mission will have an astrometric uncertainty of $\sigma_{\text{inst}} \approx 35$ microarcsecond per epoch at $m_V \approx 12$ for its best targets, with an average of 83 epochs per target⁴. From a search of the USNO-B1 catalog, we find that $\sim 5 \times 10^6$ stars are covered at this precision (Monet et al. 2003). For these targets, Gaia's S_{min} is $\sim 260 \mu\text{as}$ because coverage of 10^6 stars requires S/N ~ 5 to avoid false positives; this precision is too low to detect intermediate-mass subhalos. Orders of magnitude more stars are covered by Gaia at lower precision, but an extremely large (and very unlikely) subhalo mass would be required to produce detectable lensing at those precisions. Although there remains a small probability that Gaia could see a lens, we conclude that Gaia's astrometric precision is probably insufficient for a useful all-sky subhalo search. That said, it is prudent to at least attempt a subhalo lens search using the Gaia dataset, as the data will be available and can be readily searched for such signals.

For the N-body simulation-based lensing probabilities discussed in section 4.3.2, where typical lensing probabilities are $\sim 10^{-11}$ at $S_{\text{min}} = 5 \mu\text{as}$, much improved instrumentation capabilities would be required for detection. The only currently

⁴ [http://www.rssd.esa.int/index.php?project=\\$GAIA&page=\\$Science_Per](http://www.rssd.esa.int/index.php?project=$GAIA&page=$Science_Per)

planned instrument capable of reaching $S_{\min} = 5 \mu\text{as}$ routinely is SIM, but SIM will at most cover tens of thousands of targets during its lifetime (Unwin et al. 2008). If the subhalo mass functions derived from simulations are correct, a SIM-precision all-sky search would have to cover 10^{11} targets to have a good chance of making a detection. This capability will most certainly not be available in the near future. However, it is worth stating that a SIM-precision mission covering 10^8 targets (a possible capability for a next-generation all-sky astrometric survey), would place unique constraints on the subhalo mass function. In particular, such a survey could usefully evaluate if the simulations under-predict the subhalo mass function or if the subhalos are more dense than expected (the scenario in Fig. 8).

Similar conclusions can be drawn for blind searches of subareas of the sky: current and planned astrometric capabilities are insufficient for a large-area survey for subhalo lenses. However, if a local subhalo is suspected on the basis of other detection methods, targeted surveys are capable of either detecting the lens directly or stringently constraining its properties.

5.3. Targeted Observations

If we have some idea of where a lens might be, searching for that lens becomes much easier. For example, it has been suggested that the Fermi Large Area Telescope (Atwood et al. 2009) could detect subhalos in gamma-ray emission (e.g., Siegal-Gaskins 2008; Ando 2009; Buckley & Hooper 2010). Fermi’s first point source catalog (Abdo et al. 2010) contains a large number of unidentified sources that could be subhalos capable of producing detectable lensing signals (Buckley & Hooper 2010). Sources in the Fermi point-source catalog are localized to 6 arcminutes (median; 95% confidence) or even 1.5 arcminutes (best 50 sources; 95% confidence). The lensing search therefore requires coverage of only 0.01 sq. degrees or less. Furthermore, since Fermi has many plausible sources, we can pick the targets with the best likelihood of detection, such as sources close to the Galactic plane with many astrometric target stars. The aim here is to place the best possible limits on the lens properties (with the possibility of an actual detection), and even current techniques (reaching $S_{\min} \approx 50 \mu\text{as}$) could place useful limits on the lens properties. If astrometric lensing is detected around a gamma-ray source, then the magnitude of the deflection provides a measurement of the subhalo’s central density; the shape of the image’s path provides information about the inner density profile; and the rate of change in the image’s position provides information about v_T/d_L . If no lensing is detected, constraints could be placed on a combination of the object’s distance, mass, and density profile.

Since it is unlikely that we will know the exact position of a suspected subhalo, moderately wide-field astrometric techniques are favored for this type of search. From space, the Hubble Space Telescope (HST) has demonstrated ~ 1 mas precision crowded-field astrometry in the cores of globular clusters using the Advanced Camera for Surveys (ACS) instrument (e.g., Anderson & van der Marel 2010). However, much better precision has been demonstrated on arcminute scales from the ground.

AO-equipped 5-10m telescopes routinely achieve $100 \mu\text{as}$ precision astrometry (Cameron et al. 2009; Lu et al. 2009). These techniques minimize systematics by observing in narrow NIR bands, at consistent air masses, and with careful attention to other sources of systematic error. Such surveys re-

quire only a field with several stars within an arcminute field of view (such as is common in the galactic plane) and a few minutes of observing time per field. Using these techniques, relatively small 2m-class telescopes equipped with low-cost adaptive optics systems can reach 50-100 μas precision in tens of minutes and can perform large, intensive astrometric surveys (Britton et al. 2008; Baranec et al. 2009; Law et al. 2009). The precision can be further improved; in the absence of systematics, a 10m-class telescope is predicted to reach $10 \mu\text{as}$ in similar integration times (although currently systematics limit precisions to the $\sim 100 \mu\text{as}$ level, development is continuing). On the same basis, a 30m-class telescope could reach few- μas precision in a few minutes over a small field (Cameron et al. 2009), although the systematic errors are again likely to dominate such observations until technique improvements are made.

Current ground-based techniques with precisions of 50-100 μas can detect S_{\min} down to $\sim 200 \mu\text{as}$ with $S/N=3$. This precision may be enough to detect nearby large subhalos ($M_{\text{vir}} \gtrsim 5 \times 10^7 M_{\odot}$ or $M_{0.1\text{pc}} \gtrsim 400 M_{\odot}$ for $\gamma \geq 1.8$) in the galactic plane with current instruments. If the astrometric accuracy is improved, current 10m-class telescopes could potentially reach $S_{\min} < 50 \mu\text{as}$ in 10-minute observations. In crowded regions, such a system performing a long-term astrometric survey could detect subhalos down to stripped masses ($m_{\text{bd}} = 0.001$) of $\sim 1000 M_{\odot}$ at ~ 50 pc distances, while 30m-class telescopes could detect subhalos at least an order of magnitude smaller.

SIM offers another possible route for subhalo lens confirmation. The instrument can reach a best precision of $1 \mu\text{as}$ (and so a detectable S_{\min} of $\sim 5 \mu\text{as}$). Crowding limits require that SIM’s target stars are separated by at least ~ 5 arcseconds from each other, and so the lensing area must subtend at least ~ 25 sq. arcseconds. With these capabilities, SIM would be capable of confirming a lens 50 pc away down to a stripped virial mass of $\sim 100 M_{\odot}$ (for $\gamma = 2.0$ or 1.8), or equivalently $M_{0.1\text{pc}}$ of $10 M_{\odot}$ (Fig. 7). Because SIM is a pointed mission, it can target faint ($m_V=20$) stars at the cost of observing time, making it relatively easy to obtain a sufficient sample of stars near to a putative subhalo position. Although it may not be possible to obtain $1 \mu\text{as}$ precision observations of all stars near to a suspected lens because of observation time constraints, we estimate that S_{\min} of 4-18 μas would be obtainable in modest amounts (weeks) of SIM observation time. SIM observations could thus confirm suspected subhalos near the galactic plane down to stripped subhalo masses ($m_{\text{bd}} = 0.001$) of hundreds of solar masses or $M_{0.1\text{pc}}$ of tens of solar masses.

6. SUMMARY AND CONCLUSIONS

When a dark matter subhalo moves relative to a more distant star, the star’s apparent position changes due to gravitational lensing. By studying the image motion generated by subhalos with isothermal and NFW density profiles, we have determined that the change in the image’s position is detectable only if the subhalo’s center passes by the star with a small impact parameter ($\lesssim 0.01$ pc in the lens plane). Therefore, only the inner 0.1 pc of a subhalo is relevant for astrometric lensing, and we adopt a general power-law density profile in this region. We used the findings of the Aquarius simulation (Springel et al. 2008) to derive a relationship between the concentration of local subhalos and their virial masses, which allows us to convert between a subhalo’s virial mass and the mass enclosed within 0.1 pc of the subhalo center. We found that the image paths due to lensing by a subhalo with

$\rho \propto r^{-\gamma}$ depend strongly on γ , with cusper profiles producing much larger deflections than shallower profiles. For $\gamma \gtrsim 1.5$, an intermediate-mass subhalo ($M_{\text{vir}} \gtrsim 10^5 M_{\odot}$) within a kpc of the Sun can produce astrometric deflections that are detectable by current and near-future instruments.

We have designed an observing strategy that can be used to detect subhalo lensing in data from typical astrometric surveys (such as Gaia, SIM, or ground-based methods). The setup makes use of the typical subhalo lensing signature: the image starts out essentially fixed in position, and as the subhalo center passes by, the star rapidly moves to a new position. The star's image then remains nearly stationary for the next several years. Under our observing scheme, a star's position, proper motion, and parallax is measured during an initial calibration period, and then the star is monitored over the next several years. We define the lensing signal as the difference between the lensed trajectory and the path predicted by the measured proper motion and parallax. This strategy is immune to the most important false-positive possibilities: eccentric binary stars and point-source microlensing.

The magnitude of the resulting astrometric signal depends on the impact parameter between the subhalo and the star. For a given minimal signal required for detection, a given subhalo will detectably lens all stars within a certain area on the sky. We computed this cross section for lensing as a function of both the subhalo virial mass and the mass enclosed within 0.1 pc for several values of γ . Combining these cross sections with a local subhalo number density allows us to calculate the probability that a given star's image will be detectably deflected by a subhalo within a given observation time. To evaluate the subhalo lensing probability predicted by N-body simulations, we derive a mass function for local subhalos based on the findings of the Aquarius simulation (Springel et al. 2008).

Finally, we use these cross sections and event rates to evaluate the detectability of subhalo lensing signatures. We consider two scenarios: 1) a large-area survey for subhalo lenses

and 2) a confirmation of a subhalo suspected on the basis of other detection methods. We find that Gaia all-sky astrometric measurements are close to being able to constrain subhalos with abnormally high central densities, as could arise if substructure formed very early (Ricotti & Gould 2009; Berezhinsky et al. 2010). A subhalo's astrometric lensing signature would also be enhanced if it contains a black hole (Bertone et al. 2005; Ricotti & Gould 2009); the black hole would steepen the inner density profile and would add a point mass to the subhalo center, resulting in a distinctive astrometric lensing signature. Given these possibilities, it is certainly prudent to attempt a subhalo lensing search using Gaia, and we leave a thorough investigation of these more exotic scenarios for future work. Unfortunately, a full-sky survey with much higher astrometric precision than Gaia is required to usefully constrain the dark matter subhalo mass function currently predicted by N-body simulations.

A targeted search for astrometric lensing by subhalos is far more promising; if a subhalo's presence is suspected by other means (for example, as a Fermi gamma-ray source) current and near-future ground based astrometry surveys are capable of directly searching for the subhalo's lensing signature, down to stripped masses ($0.001 M_{\text{vir}}$) of $\sim 1000 M_{\odot}$ at ~ 50 pc distances. The SIM astrometric satellite could confirm suspected subhalos near the galactic plane even if the subhalo is 1-2 orders of magnitude less massive or more distant. Fermi has already observed gamma-ray sources of unknown origin, and the possibility that these sources are dark matter subhalos has been investigated (Buckley & Hooper 2010). If Fermi detects a gamma-ray source that is consistent with a nearby intermediate-mass subhalo, then high-precision astrometry could at a minimum constrain the object's distance, mass, and density profile, and it may even provide definitive confirmation for the detection of dark matter substructure.

We thank Niayesh Afshordi, Latham Boyle, Marc Kamionkowski, Annika Peter, and Kris Sigurdson for useful discussions and comments on the manuscript.

APPENDIX

STRONG LENSING AND TRUNCATION EFFECTS

The lensing cross sections presented in Section 4.2 confirm that we are firmly in the weak-lensing regime ($\alpha \ll \beta$ in Fig. 1). It follows from Eq. (23) that the condition $\alpha \ll \beta$ is equivalent to the condition $\theta_E \ll \beta$. In our coordinate system, with the lens moving along the x -axis, the minimal value for β is the impact parameter β_y ; we are in the weak-lensing regime only if $\theta_E \ll \beta_y$. We should excise the area with $\theta_E \geq \beta_y$ from our cross sections because our solution to the lens equation is not valid in this region. If $\Delta\beta$ is the angular distance traversed by the lens during the observation period, then the area that should be excised is $A_x = 2\Delta\beta \times \theta_E$. This area is much smaller than the total cross section for lensing, $A = 2(\Delta\beta)^2 A_g$ from Eq. (35), if $\Delta\beta \gg \theta_E/A_g$. For all the subhalos that we consider ($M_{\text{vir}} < 10^8 M_{\odot}$, $\gamma \leq 2$), $\theta_E/A_g \lesssim 10 \mu\text{as}$. With this bound and $v_T > 5$ km/s, $\Delta\beta \gg \theta_E/A_g$ is satisfied if $d_L \ll 1000$ kpc. We therefore conclude that A_x is an insignificant contribution to the lensing cross section and we need not exclude it.

The cross section for lensing also tells us how far a star may be from the center of the subhalo and still be detectably deflected. As discussed in Section 2.3, we do not truncate the density profile when calculating the surface density of the subhalo, and this approximation is valid only if ξ is much smaller than the truncation radius (R_t) of the subhalo. In Section 2.3 we stated that this condition is safely satisfied if $R_t \gtrsim 0.1$ pc, and we will now verify that claim. We assume that we are only interested in subhalos with virial masses less than $10^8 M_{\odot}$ and signals greater than $1 \mu\text{as}$. These restrictions define a lower bound on detectable values of the geometric signal; for $\gamma = \{2.0, 1.8, 1.5, 1.2\}$, we have $S_g > \{0.0020, 0.0056, 0.098, 1.22\}$. At these small values, S_g is nearly independent of the phase φ , as illustrated in the left panel of Fig. 6. Since φ is confined to be between 0 and 1, the maximal value of $\tilde{\beta}$ that keeps S_g above these lower bounds is just the area A_g evaluated at the minimal value of S_g : for $\gamma = \{2.0, 1.8, 1.5, 1.2\}$, we have $\tilde{\beta} < \{37, 28, 10, 0.2\}$. From the definition of $\tilde{\beta}$, we see that $\xi_y = v_T t_{\text{obs}} \tilde{\beta}$, and so the maximal distance (in the lens plane) between the star and the subhalo center is $\xi_{\text{max}} = v_T t_{\text{obs}} \sqrt{1 + \tilde{\beta}_{\text{max}}^2}$. With $t_{\text{obs}} = 4$ years, and $v_T = 200$ km/s, we have $\xi_{\text{max}} = \{0.03, 0.02, 0.008, 0.0008\}$ pc for $\gamma = \{2.0, 1.8, 1.5, 1.2\}$. If we take $R_t \gtrsim 0.1$ pc, then ignoring the truncation of the density profile overestimates $M_{2D}(\xi_{\text{max}})$ by less than 20% for $\gamma \geq 1.5$ and less than 40% for $\gamma = 1.2$. Moreover, these are

very conservative estimates; for $M_{\text{vir}} \ll 10^8 M_\odot$ or $S_{\text{min}} \gg 1 \mu\text{as}$, the minimal values of S_g will be much larger, leading to smaller values of ξ_{max} and less disparity between the truncated and infinite values of $M_{2D}(\xi_{\text{max}})$.

SUBHALO PROPERTIES

We are interested in intermediate-mass subhalos ($10 M_\odot \lesssim M_t \lesssim 10^6 M_\odot$) that are located within a few kpc of the Sun. Fortunately, numerical simulations have recently reached the resolutions required to probe substructure within a few kpc of the Sun (Springel et al. 2008; Diemand et al. 2008), with minimum resolvable subhalo masses of $\sim 10^5 M_\odot$. In this appendix, we will use the Aquarius simulation results presented by Springel et al. (2008) to derive a mass function and a concentration-mass relation for these local subhalos.

The Aquarius simulation suite includes simulations of six galaxy-size dark matter halos with $\sim 2 \times 10^8$ particles in each halo and a higher resolution simulation of one of these six halos (Aq-A) with 1.4×10^9 particles. In the Aq-A simulation, each particle has a mass of $1712 M_\odot$, making it possible to identify subhalos with masses greater than $10^5 M_\odot$. Springel et al. (2008) defines the interior of the host halo as a sphere with a mean density that is 50 times the critical density; the radius of this sphere called r_{50} , and the mass enclosed is M_{50} . The Aq-A halo has $M_{50} = 2.5 \times 10^{12} M_\odot$ and $r_{50} = 433.5$ kpc. The mass of a subhalo (M_t) is determined by the SUBFIND algorithm (Springel et al. 2001), which counts the number of gravitationally bound particles and then multiplies by the mass per particle to obtain M_t . We will continue to use $M_t \equiv m_{\text{bd}} M_{\text{vir}}$ to parameterize the effects of tidal stripping on the subhalo's mass.

Subhalo Mass Function

The subhalo mass function measured in the Aq-A halo for all subhalos with $r < r_{50}$ is

$$\frac{dN}{dM_t} = a_0 \left(\frac{M_t}{m_0} \right)^{-1.9}, \quad (\text{B1})$$

with $a_0 = 8.21 \times 10^7 M_{50}^{-1}$ and $m_0 = 10^{-5} M_{50}$. Springel et al. (2008) also report that the subhalo number density has the same spatial dependence for all subhalo masses $10^5 M_\odot \leq M_t \leq 10^{10} M_\odot$:

$$n(M, r) = n_0(M) \exp \left[-\frac{2}{\alpha} \left\{ \left(\frac{r}{0.46 r_{50}} \right)^\alpha - 1 \right\} \right] \quad (\text{B2})$$

with $\alpha = 0.678$. To determine the function dn_0/dM_t , we integrate Eq. (B2) over $r < r_{50}$ and match the result to Eq. (B1). The resulting mass function is

$$\frac{dn}{dM_t} = \frac{a_0}{1.985 r_{50}^3} \left(\frac{M_t}{m_0} \right)^{-1.9} \exp \left[-\frac{2}{\alpha} \left\{ \left(\frac{r}{0.46 r_{50}} \right)^\alpha - 1 \right\} \right]. \quad (\text{B3})$$

The Aq-A halo is larger than the Milky Way's halo (e.g., Dehnen et al. 2006; Li & White 2008; Xue et al. 2008; Reid et al. 2009), so we must use appropriate values of r_{50} and M_{50} when evaluating Eq. (B3). We use the density profile presented by Xue et al. (2008) to derive approximate values of r_{50} and M_{50} for the Milky Way: $M_{50} \simeq 9.5 \times 10^{11} M_\odot$ and $r_{50} \simeq 310$ kpc. With these parameters,

$$\frac{dn}{dM_t} = \frac{2.5 \times 10^{-8}}{\text{pc}^3 M_\odot} \left(\frac{M_t}{M_\odot} \right)^{-1.9} \exp \left[-\frac{2}{\alpha} \left\{ \left(\frac{r}{140 \text{ kpc}} \right)^\alpha - 1 \right\} \right]. \quad (\text{B4})$$

For $r \lesssim 20$ kpc, the subhalo number density is no longer strongly dependent on r , and it changes by only 7% as you move 2 kpc away from the solar radius ($R_0 \simeq 8$ kpc). We will neglect these small variations so that we may treat the local subhalo number density as isotropic. If we evaluate Eq. (B4) at $r = 8$ kpc, we find

$$\frac{dn}{dM_t} = \frac{3 \times 10^{-7}}{\text{pc}^3 M_\odot} \left(\frac{M_t}{M_\odot} \right)^{-1.9}. \quad (\text{B5})$$

We now need to convert this mass function for subhalo mass M_t to a mass function for virial mass M_{vir} . We will assume that all subhalos within 2 kpc of the Sun lose the same fraction of their mass due to tidal stripping. If $M_t = m_{\text{bd}} M_{\text{vir}}$, where m_{bd} is constant, then we have

$$\frac{dn}{dM_{\text{vir}}} = \frac{3 \times 10^{-7} m_{\text{bd}}^{-0.9}}{\text{pc}^3 M_\odot} \left(\frac{M_{\text{vir}}}{M_\odot} \right)^{-1.9}. \quad (\text{B6})$$

There is great uncertainty surrounding the local value for m_{bd} . Diemand et al. (2007b) monitored subhalo mass evolution in the Via Lactea simulation, and unsurprisingly found that the fraction of mass lost due to tidal stripping increases closer to the center of the host halo. They found that subhalos in the region containing the inner sixth of the host halo mass lose roughly 80% of their mass between a redshift $z \sim 2$ and the present day. This sample contains subhalos that are far further from the host's center than the Sun, so we may consider $m_{\text{bd}} \simeq 0.2$ to be a rough upper bound. Meanwhile, van den Bosch et al. (2005) developed a semi-analytical model for tidal stripping and concluded that $0.001 \lesssim m_{\text{bd}} \lesssim 0.1$ for all subhalos in a Milky-Way sized host, with most subhalos losing 99% of their original virial mass. Finally, Eq. (B6) implies that the total mass in a sphere with radius 2 kpc that was once part of a subhalo with $M_{\text{vir}} \lesssim 10^8 M_\odot$ is $6m_{\text{bd}}^{-0.9} \times 10^5 M_\odot$. This mass must be less than all the dark matter contained

in this sphere ($3.5 \times 10^8 M_\odot$), so $m_{\text{bd}} \gtrsim 0.001$ on average. We adopt a middle-of-the-road value of $m_{\text{bd}} = 0.01$ for local subhalos when evaluating the lensing event rates in Section 4.3.2. This value for m_{bd} does not include stripping by stellar encounters; here M_t is the subhalo mass measured in N-body simulations that do not include stars.

Subhalo Concentrations

Many methods for assigning concentrations to dark matter halos have been proposed (e.g. Bullock et al. 2001; Neto et al. 2007; Duffy et al. 2008; Macciò et al. 2008), but these models focus on isolated halos that are far more massive than the subhalos we consider. Furthermore, numerical simulations indicate that subhalos nearer to the center of the host halo have higher concentrations than both isolated halos (Ghigna et al. 1998; Bullock et al. 2001) and subhalos in the outskirts of the host halo (Diemand et al. 2007b; Springel et al. 2008; Diemand et al. 2008). In light of this distinction, we adopt a $c(M_{\text{vir}})$ relation for local subhalos that is based on the findings of the Aquarius simulation (Springel et al. 2008). Since the virial radius of a subhalo is not easily measured, a different concentration parameter is often used to characterize the concentration of subhalos in simulations:

$$\delta_V \equiv \frac{2V_{\text{max}}^2}{(H_0 r_{\text{max}})^2}, \quad (\text{B7})$$

where V_{max} is the maximum circular velocity within the subhalo, and r_{max} is the distance from the subhalo center at which the circular velocity is maximized. The Aquarius team found that δ_V depends on subhalo mass M_t and distance from the host halo center r ; when they average over all subhalos with $M_t \gtrsim 3 \times 10^6 M_\odot$, they find

$$\delta_V = 3.8 \times 10^6 \left(\frac{r}{\text{kpc}} \right)^{-0.63}, \quad (\text{B8})$$

and when they average over all subhalos, they find⁵

$$\delta_V = 5.8 \times 10^4 \left(\frac{M_t}{10^8 M_\odot} \right)^{-0.18}, \quad (\text{B9})$$

with considerable scatter in both cases (Springel et al. 2008). Inspired by these relations, we adopt a model

$$\delta_V = N_\delta \left(\frac{r}{\text{kpc}} \right)^{-0.63} \left(\frac{M_t}{10^8 M_\odot} \right)^{-0.18}, \quad (\text{B10})$$

and we use the position-dependent subhalo mass function derived in the previous subsection to compare this model with Eqs. (B8) and (B9). Matching Eq. (B8) gives $N_\delta = 2.4 \times 10^6$, while matching Eq. (B9) gives $N_\delta = 1.5 \times 10^6$. Since increasing the subhalo concentration enhances the lensing signal, we adopt the latter value to be conservative.

Given a full (pre-stripped) density profile for the subhalo, it is possible to relate δ_V to $c \equiv R_{\text{vir}}/r_{-2}$, where r_{-2} is the radius at which $d \ln \rho / d \ln r = -2$ (e.g., Diemand et al. 2007b). For the density profile given by Eq. (25),

$$\delta_V = \left[\frac{\bar{\rho}_{\text{vir}}(z_v)}{\rho_{\text{crit},0}} \right] \left(\frac{c}{y_{\text{max}}} \right)^3 \frac{B[y_{\text{max}}(\gamma - 2); 3 - \gamma, \gamma - 2]}{B[c(\gamma - 2); 3 - \gamma, \gamma - 2]}, \quad (\text{B11})$$

where z_v is the redshift at which R_{vir} is evaluated, $\rho_{\text{crit},0}$ is the present-day critical density, $y_{\text{max}} \equiv r_{\text{max}}/r_{-2}$, and $B[z; a, b]$ is the incomplete Beta function. For $1 \leq \gamma < 2$, $y_{\text{max}} \simeq 2.1$, and the function $\delta_V(c)$ is not strongly dependent on γ . Since we are interested in subhalos with $10^4 M_\odot < M_{\text{vir}} < 10^8 M_\odot$ and $r \simeq 8$ kpc, we only need to consider the range $10^5 < \delta_V < 10^7$. In this range, $\delta_V(c)$ is well-approximated by a simple power law:

$$\delta_V \simeq 0.049 \left[\frac{\bar{\rho}_{\text{vir}}(z_v)}{\rho_{\text{crit},0}} \right] c^{2.67}. \quad (\text{B12})$$

We obtain a final expression for $c(M_{\text{vir}})$ by inverting Eq. (B12) and inserting Eq. (B10). With $N_\delta = 1.5 \times 10^6$, we find

$$c = 94 m_{\text{bd}}^{-0.067} \left(\frac{\bar{\rho}_{\text{vir}}(z_v)}{4.6 M_\oplus \text{pc}^{-3}} \right)^{-0.37} \left(\frac{M_{\text{vir}}}{10^6 M_\odot} \right)^{-0.067} \left(\frac{r}{8 \text{ kpc}} \right)^{-0.24}, \quad (\text{B13})$$

where we have defined $m_{\text{bd}} \equiv M_t/M_{\text{vir}}$. Since $c(M_{\text{vir}})$ changes little for $0.01 < m_{\text{bd}} < 1$, we will take $m_{\text{bd}} = 1$ when evaluating the concentration. The dependence of $c(M_{\text{vir}})$ on the subhalo's location is also fairly weak; for a fixed value of M_{vir} , c decreases by only 10% between $8 \text{ kpc} < r < 13 \text{ kpc}$ and increases by only 25% between $3 \text{ kpc} < r < 8 \text{ kpc}$. We conservatively take $r = 8$ kpc when evaluating the concentration of local subhalos. Finally, we note that subhalos in simulations that include baryons tend to be more concentrated than subhalos in simulations without baryons (Romano-Díaz et al. 2010), so it is possible that our model underestimates the concentration of local subhalos.

REFERENCES

⁵ The exponent is reported incorrectly in the caption of Fig. 28 of Springel et al. (2008), but the curve shown in Fig. 28 is correct.

- Amara, A., Metcalf, R. B., Cox, T. J., & Ostriker, J. P. 2006, *MNRAS*, 367, 1367
- Anderson, J. & van der Marel, R. P. 2010, *ApJ*, 710, 1032
- Ando, S. 2009, *Phys. Rev. D*, 80, 023520
- Atwood, W. B., et al. (Fermi collaboration) 2009, *ApJ*, 697, 1071
- Baranec, C., Dekany, R., Kulkarni, S. R., Law, N. M., Ofek, E., Kasliwal, M., & Velur, V. 2009, in *astro2010: The Astronomy and Astrophysics Decadal Survey*, 14
- Bartelmann, M. 1996, *A&A*, 313, 697
- Berezinsky, V., Dokuchaev, V., & Eroshenko, Y. 2006, *Phys. Rev. D*, 73, 063504
- Berezinsky, V., Dokuchaev, V., Eroshenko, Y., Kachelrieß, M., & Solberg, M. A. 2010, *Phys. Rev. D*, 81, 103529
- Bergström, L., Edsjö, J., Gondolo, P., & Ullio, P. 1999, *Phys. Rev. D*, 59, 043506
- Bertone, G., Zentner, A. R., & Silk, J. 2005, *Phys. Rev. D*, 72, 103517
- Britton, M., Velur, V., Law, N., Choi, P., & Penprase, B. E. 2008, *Proc. SPIE*, 7015, 701516
- Bryan, G. L. & Norman, M. L. 1998, *ApJ*, 495, 80
- Bryan, S. E., Mao, S., & Kay, S. T. 2008, *MNRAS*, 391, 959
- Buckley, M. R. & Hooper, D. 2010, *Phys. Rev. D*, 82, 063501
- Bullock, J. S., Kolatt, T. S., Sigad, Y., Somerville, R. S., Kravtsov, A. V., Klypin, A. A., Primack, J. R., & Dekel, A. 2001, *MNRAS*, 321, 559
- Calcáneo-Roldán, C. & Moore, B. 2000, *Phys. Rev. D*, 62, 123005
- Cameron, P. B., Britton, M. C., & Kulkarni, S. R. 2009, *AJ*, 137, 83
- Chen, J., Rozo, E., Dalal, N., & Taylor, J. E. 2007, *ApJ*, 659, 52
- Chen, X., Kamionkowski, M., & Zhang, X. 2001, *Phys. Rev. D*, 64, 021302
- Chiba, M. 2002, *ApJ*, 565, 17
- Congdon, A. B., Keeton, C. R., & Nordgren, C. E. 2010, *ApJ*, 709, 552
- Dalal, N. & Kochanek, C. S. 2002, *ApJ*, 572, 25
- Dehnen, W., McLaughlin, D. E., & Sachania, J. 2006, *MNRAS*, 369, 1688
- Diemand, J., Kuhlen, M., & Madau, P. 2007a, *ApJ*, 657, 262
- . 2007b, *ApJ*, 667, 859
- Diemand, J., Kuhlen, M., Madau, P., Zemp, M., Moore, B., Potter, D., & Stadel, J. 2008, *Nature*, 454, 735
- Diemand, J., Moore, B., & Stadel, J. 2005, *Nature*, 433, 389
- D'Onghia, E., Springel, V., Hernquist, L., & Keres, D. 2010, *ApJ*, 709, 1138
- Drukier, A. K., Freese, K., & Spergel, D. N. 1986, *Phys. Rev. D*, 33, 3495
- Duffy, A. R., Schaye, J., Kay, S. T., & Dalla Vecchia, C. 2008, *MNRAS*, 390, L64
- Dupuy, T. J., Liu, M. C., & Bowler, B. P. 2009, *ApJ*, 706, 328
- Gao, L., De Lucia, G., White, S. D. M., & Jenkins, A. 2004, *MNRAS*, 352, L1
- Gaudi, B. S. & Bloom, J. S. 2005, *ApJ*, 635, 711
- Ghigna, S., Moore, B., Governato, F., Lake, G., Quinn, T., & Stadel, J. 1998, *MNRAS*, 300, 146
- . 2000, *ApJ*, 544, 616
- Gillessen, S., Eisenhauer, F., Trippe, S., Alexander, T., Genzel, R., Martins, F., & Ott, T. 2009, *ApJ*, 692, 1075
- Goerdt, T., Gnedin, O. Y., Moore, B., Diemand, J., & Stadel, J. 2007, *MNRAS*, 375, 191
- Golse, G. & Kneib, J. 2002, *A&A*, 390, 821
- Gould, A. 2000, *ApJ*, 532, 936
- Green, A. M. & Goodwin, S. P. 2007, *MNRAS*, 375, 1111
- Hayashi, E., Navarro, J. F., Taylor, J. E., Stadel, J., & Quinn, T. 2003, *ApJ*, 584, 541
- Helminiak, K. G., Konacki, M., Kulkarni, S. R., & Eisner, J. 2009, *MNRAS*, 400, 406
- Henry, T. J., Money, D. G., Shankland, P. D., Reid, M. J., van Altena, W., & Zacharias, N. 2009, in *astro2010: The Astronomy and Astrophysics Decadal Survey*, 123
- Hu, W., Barkana, R., & Gruzinov, A. 2000, *Physical Review Letters*, 85, 1158
- Inoue, K. T. & Chiba, M. 2005a, *ApJ*, 634, 77
- . 2005b, *ApJ*, 633, 23
- Ireland, M. J., Kraus, A., Martinache, F., Lloyd, J. P., & Tuthill, P. G. 2008, *ApJ*, 678, 463
- Ishiyama, T., Makino, J., & Ebisuzaki, T. 2010, *ApJ*, 723, L195
- Ivezić, Ž., et al. 2008, in *IAU Symp. 248, A Giant Step: from Milli- to Micro-arcsecond Astrometry*, ed. W. J. Jin, I. Platais, & M. A. C. Perryman (Cambridge: Cambridge Univ. Press), 537
- Jackson, N., Bryan, S. E., Mao, S., & Li, C. 2010, *MNRAS*, 403, 826
- Kamionkowski, M. & Koushiappas, S. M. 2008, *Phys. Rev. D*, 77, 103509
- Kamionkowski, M., Koushiappas, S. M., & Kuhlen, M. 2010, *Phys. Rev. D*, 81, 043532
- Kazantzidis, S., Mayer, L., Mastropietro, C., Diemand, J., Stadel, J., & Moore, B. 2004, *ApJ*, 608, 663
- Keeton, C. R. & Moustakas, L. A. 2009, *ApJ*, 699, 1720
- Klypin, A., Gottlöber, S., Kravtsov, A. V., & Khokhlov, A. M. 1999a, *ApJ*, 516, 530
- Klypin, A., Kravtsov, A. V., Valenzuela, O., & Prada, F. 1999b, *ApJ*, 522, 82
- Knebe, A., Libeskind, N. I., Knollmann, S. R., Yepes, G., Gottlöber, S., & Hoffman, Y. 2010, *MNRAS*, 405, 1119
- Kochanek, C. S. & Dalal, N. 2004, *ApJ*, 610, 69
- Konopacky, Q. M., Ghez, A. M., Barman, T. S., Rice, E. L., Bailey, J. I., White, R. J., McLean, I. S., & Duchêne, G. 2010, *ApJ*, 711, 1087
- Koopmans, L. V. E. 2005, *MNRAS*, 363, 1136
- Koopmans, L. V. E., Garrett, M. A., Blandford, R. D., Lawrence, C. R., Patnaik, A. R., & Porcas, R. W. 2002, *MNRAS*, 334, 39
- Kravtsov, A. V., Gnedin, O. Y., & Klypin, A. A. 2004, *ApJ*, 609, 482
- Kuhlen, M., Diemand, J., & Madau, P. 2007, *ApJ*, 671, 1135
- Law, N. M., Kulkarni, S. R., Dekany, R. G., & Baranec, C. 2009, in *astro2010: The Astronomy and Astrophysics Decadal Survey*, 173
- Lee, C. H., Seitz, S., Riffeser, A., & Bender, R. 2010, *MNRAS*, 407, 1597
- Li, Y. & White, S. D. M. 2008, *MNRAS*, 384, 1459
- Lindgren, L., et al. 2008, in *IAU Symp. 248, A Giant Step: from Milli- to Micro-arcsecond Astrometry*, ed. W. J. Jin, I. Platais, & M. A. C. Perryman (Cambridge: Cambridge Univ. Press), 217
- Lu, J. R., Ghez, A. M., Hornstein, S. D., Morris, M. R., Becklin, E. E., & Matthews, K. 2009, *ApJ*, 690, 1463
- Macciò, A. V., Dutton, A. A., & van den Bosch, F. C. 2008, *MNRAS*, 391, 1940
- Macciò, A. V., Moore, B., Stadel, J., & Diemand, J. 2006, *MNRAS*, 366, 1529
- Madau, P., Diemand, J., & Kuhlen, M. 2008, *ApJ*, 679, 1260
- Malbet, F., et al. 2010, in *Astronomical Society of the Pacific Conference Series*, Vol. 430, *Astronomical Society of the Pacific Conference Series*, ed. V. Coudé Du Foresto, D. M. Gelino, & I. Ribas, 84
- Mao, S., Jing, Y., Ostriker, J. P., & Weller, J. 2004, *ApJ*, 604, L5
- Mao, S. & Schneider, P. 1998, *MNRAS*, 295, 587
- Metcalf, R. B. 2002, *ApJ*, 580, 696
- Metcalf, R. B. & Madau, P. 2001, *ApJ*, 563, 9
- Miralda-Escude, J. 1996, *ApJ*, 470, L113+
- Monet, D. G., et al. 2003, *AJ*, 125, 984
- Moore, B., Ghigna, S., Governato, F., Lake, G., Quinn, T., Stadel, J., & Tozzi, P. 1999, *ApJ*, 524, L19
- More, A., McKean, J. P., More, S., Porcas, R. W., Koopmans, L. V. E., & Garrett, M. A. 2009, *MNRAS*, 394, 174
- Muterspaugh, M. W., Lane, B. F., Konacki, M., Burke, B. F., Colavita, M. M., Kulkarni, S. R., & Shao, M. 2006, in *Society of Photo-Optical Instrumentation Engineers (SPIE) Conference Series*, Vol. 6268, *Society of Photo-Optical Instrumentation Engineers (SPIE) Conference Series*
- Navarro, J. F., Frenk, C. S., & White, S. D. M. 1996, *ApJ*, 462, 563
- . 1997, *ApJ*, 490, 493
- Neto, A. F., et al. 2007, *MNRAS*, 381, 1450
- Paczynski, B. 1995, *Acta Astronomica*, 45, 345
- . 1998, *ApJ*, 494, L23+
- Pravdo, S. H., Shaklan, S. B., Wiktorowicz, S. J., Kulkarni, S., Lloyd, J. P., Martinache, F., Tuthill, P. G., & Ireland, M. J. 2006, *ApJ*, 649, 389
- Profumo, S., Sigurdson, K., & Kamionkowski, M. 2006, *Physical Review Letters*, 97, 031301
- Read, J. I., Wilkinson, M. I., Evans, N. W., Gilmore, G., & Kleyana, J. T. 2006, *MNRAS*, 366, 429
- Reed, D., Governato, F., Quinn, T., Gardner, J., Stadel, J., & Lake, G. 2005, *MNRAS*, 359, 1537
- Reid, M. J., et al. 2009, *ApJ*, 700, 137
- Ricotti, M. & Gould, A. 2009, *ApJ*, 707, 979
- Riehm, T., Zackrisson, E., Mörtzell, E., & Wiik, K. 2009, *ApJ*, 700, 1552
- Romano-Díaz, E., Shlosman, I., Heller, C., & Hoffman, Y. 2010, *ApJ*, 716, 1095
- Schneider, A., Krauss, L., & Moore, B. 2010, *Phys. Rev. D*, 82, 063525
- Siegal-Gaskins, J. M. 2008, *Journal of Cosmology and Astro-Particle Physics*, 10, 40
- Siegel, E. R., Hertzberg, M. P., & Fry, J. N. 2007, *MNRAS*, 382, 879
- Springel, V., et al. 2008, *MNRAS*, 391, 1685
- Springel, V., White, S. D. M., Tormen, G., & Kauffmann, G. 2001, *MNRAS*, 328, 726
- Stoehr, F., White, S. D. M., Springel, V., Tormen, G., & Yoshida, N. 2003, *MNRAS*, 345, 1313
- Subasavage, J. P., Jao, W., Henry, T. J., Bergeron, P., Dufour, P., Ianna, P. A., Costa, E., & Méndez, R. A. 2009, *AJ*, 137, 4547
- Takahashi, R. 2003, *ApJ*, 595, 418

- Unwin, S. C., et al. 2008, *PASP*, 120, 38
- van Belle, G. T., et al. (The Espri Consortium) 2008, *The Messenger*, 134, 6
- van den Bosch, F. C., Tormen, G., & Giocoli, C. 2005, *MNRAS*, 359, 1029
- Vegetti, S. & Koopmans, L. V. E. 2009a, *MNRAS*, 392, 945
- , 2009b, *MNRAS*, 400, 1583
- Walker, M. A. 1995, *ApJ*, 453, 37
- Williams, L. L. R., Foley, P., Farnsworth, D., & Belter, J. 2008, *ApJ*, 685, 725
- Xu, D. D., Mao, S., Cooper, A. P., Wang, J., Gao, L., Frenk, C. S., & Springel, V. 2010, *MNRAS*, 408, 1721
- Xu, D. D., et al. 2009, *MNRAS*, 398, 1235
- Xue, X. X., et al. 2008, *ApJ*, 684, 1143
- Yonehara, A., Umemura, M., & Susa, H. 2003, *PASJ*, 55, 1059
- Zackrisson, E., Riehm, T., Möller, O., Wiik, K., & Nurmi, P. 2008, *ApJ*, 684, 804
- Zhao, H., Hooper, D., Angus, G. W., Taylor, J. E., & Silk, J. 2007, *ApJ*, 654, 697